Journal of Computer-Aided Molecular Design
https://doi.org/10.1007/s10822-021-00414-5

Molecular mechanism of thiamine pyrophosphate import into mitochondria: a molecular simulation study

F. Van Liefferinge[1] · E.-M. Krammer[1,2] · J. Waeytens[1,3] · M. Prévost[1]

Received: 9 April 2021 / Accepted: 26 July 2021

Abstract

The import of thiamine pyrophosphate (TPP) through both mitochondrial membranes was studied using a total of 3-µs molecular dynamics simulations. Regarding the translocation through the mitochondrial outer membrane, our simulations support the conjecture that TPP uses the voltage-dependent anion channel, the major pore of this membrane, for its passage to the intermembrane space, as its transport presents significant analogies with that used by other metabolites previously studied, in particular with ATP. As far as passing through the mitochondrial inner membrane is concerned, our simulations show that the specific carrier of TPP has a single binding site that becomes accessible, through an alternating access mechanism. The preference of this transporter for TPP can be rationalized mainly by three residues located in the binding site that differ from those identified in the ATP/ADP carrier, the most studied member of the mitochondrial carrier family. The simulated transport mechanism of TPP highlights the essential role, at the energetic level, of the contributions coming from the formation and breakage of two networks of salt bridges, one on the side of the matrix and the other on the side of the intermembrane space, as well as the interactions, mainly of an ionic nature, formed by TPP upon its binding. The energy contribution provided by the cytosolic network establishes a lower barrier than that of the matrix network, which can be explained by the lower interaction energy of TPP on the matrix side or possibly a uniport activity.

Keywords Membrane channels · Membrane Transporters · Metabolite transport · Thiamine pyrophophate · Molecular dynamics

Abbreviations

AAC	ADP/ATP carrier
c-state	Cytoplasmic-open state
ffTK	Force field tool kit
IMS	Intermembrane space
m-state	Matrix-open state
MIM	Mitochondrial inner membrane
MOM	Mitochondrial outer membrane
MCF	Mitochondrial carrier family
TM	Transmembrane
TPP	Thiamine pyrophosphate
TPPT	Thiamine pyrophosphate transporter
VDAC	Voltage dependent anion channel

✉ M. Prévost
Martine.Prevost@ulb.be

[1] Structure et Fonction des Membranes Biologiques, Université Libre de Bruxelles (ULB), Brussels, Belgium

[2] Currently at Unité de glycobiologie structurale et fonctionnelle (UGSF), University Lille, CNRS, UMR 8576, Lille, France

[3] Institut de Chimie Physique d'Orsay, CNRS UMR8000, Université Paris-Sud, Université Paris-Saclay, Orsay, France

Introduction

Thiamine pyrophosphate (TPP) serves as a cofactor for several mitochondrial enzymes involved in essential metabolic reactions related to ATP production and oxidative energy metabolism [1–3]. Its deficiency has been linked to several human diseases such as Amish microencephaly, bilateral necrosis and progressive polyneuropathy [4–6].

To fulfill its role as a mitochondrial enzyme cofactor, TPP must be imported from the cytosol and must therefore pass through the two mitochondrial membranes (Fig. 1A). For passage through the mitochondrial outer membrane (MOM), the voltage-dependent anion channel (VDAC) is the most likely pathway through which TPP should be imported (Fig. 1A). VDAC is a very abundant, large pore protein known to facilitate the exchange of many inorganic ions and metabolites from the cytosol to the intermembrane

Journal : Large 10822 | Article No : 414 | Pages : 22 | MS Code : 414 | Dispatch : 11-8-2021

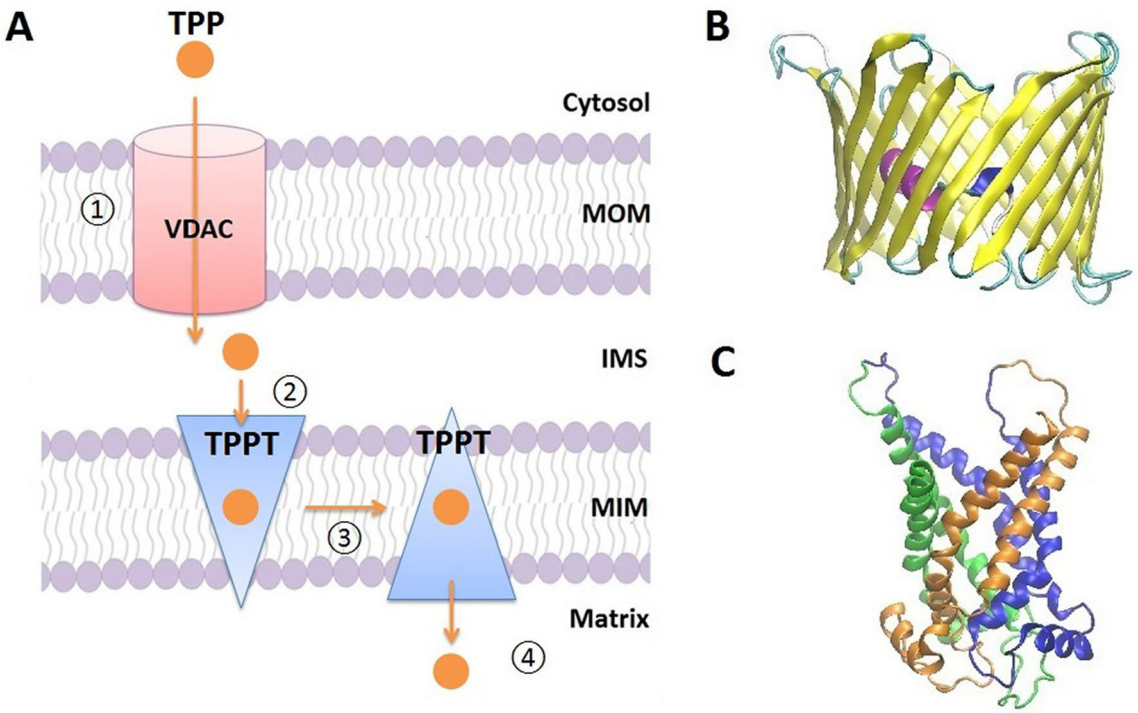

Fig. 1 TPP import into the mitochondrial matrix. **A** Schematic representation of TPP import through the two mitochondrial membranes. The pathway followed by TPP (orange sphere) is illustrated by orange arrows. (1) TPP is translocated through VDAC, the main metabolite conduit of the MOM, from the cytosol to the IMS. (2) TPP binds to the c-state of TPPT. (3) TPPT undergoes a conformational change from an c- to an m-state. (4) Unbinding of TPP from TPPT m- state and release to the matrix. **B**/**C** Side view of the 3D structure of (**B**) mVDAC1 (PDB ID: 3EMN [15]; colored according to the secondary structure) and of (**C**) bAAC, homologous to TPPT (PDB ID: 1OKC [33]: colored orange—domain 1, blue—domain 2, green—domain 3) is shown as a cartoon, respectively. Both proteins are presented with their cytosolic side upwards

space (IMS) and vice versa and as such to control much of the permeability of MOM [7–9]. All organisms with mitochondria share at least one VDAC isoform with similar electrophysiological properties (such as conductance, voltage-dependence and selectivity) [10–12]. The 3D structure of VDAC of different species (human, mouse and zebrafish) has been determined using either NMR, X-ray crystallography, or a combination of both methods [13–19]. These structures present a large open β-barrel made of 19 β-strands and one N-terminal helical segment folded inside the barrel (Fig. 1B). Although the biological relevance of this fold has been debated [20, 21], most of the findings from structural and functional studies have confirmed the validity of these structures rationalizing important VDAC properties [9, 16, 22–29]. In contrast to the MOM, the mitochondrial inner membrane (MIM) is impermeable except through specific transporters. Uptake of TPP by the MIM occurs via a specific carrier, the TPP transporter (TPPT; Fig. 1), which belongs to the mitochondrial carrier family (MCF) [5, 6, 30]. Like many other transporters [31], MCF proteins operate via the alternating access mechanism [32] during which the protein undergoes a transition between two conformations, the first open to the IMS (c-state) and the second open to the mitochondrial matrix (m-state). Those conformations open or close the binding site with the aid of specific gating residues to keep the substrate exposed to only one side of the membrane at a time. No TPPT 3D structure has been determined so far and most of the structural information on the MCF comes from crystallographic studies of the ADP/ATP carrier (AAC). All but one of the resolved AAC structures adopt a c-state thanks to the use of an inhibitor (carboxyatractyloside) blocking the protein in this state [33–35]. Recently, the structure of the m-state was solved in complex with a specific inhibitor (bongekric acid) and a nanobody [36]. All AAC structures feature three domains of about 100 amino acids each related by threefold pseudo-symmetry and made of two transmembrane (TM) α-helices joined by a large hydrophilic segment (Fig. 1C) [37]. The gating mechanism of AAC involves a network of salt bridges on both the IMS and the matrix sides that need to break or form to allow alternate access to the central binding site during the transport cycle [33, 36, 37]. MCF proteins mainly transport negatively charged substrates [38]. Most of them work as antiporters. However, a few function as uniporters or proton symporters or even a combination of these transport mechanisms [38]. Yeast TPPT has been shown to transport

Journal : Large 10822 | Article No : 414 | Pages : 22 | MS Code : 414 | Dispatch : 11-8-2021

TPP or TMP by both uniport and exchange [39] while both the human and *D. melanogaster* transporters only catalyze exchange of TPP and in addition for the human transporter exchange of TMP [6].

In this study, we have investigated, using different molecular dynamics (MD) techniques, the mechanism by which TPP is imported from the cytosol into the mitochondrial matrix. Our simulation data show that TPP is likely to cross the MOM through VDAC. This crossing is favored by the formation of ionic interactions with basic residues, most of which are conserved from one species to another. The permeation path of TPP has marked similarities with that of other analog metabolites [9]. As for its transport through the MIM, TPP is attracted to a body of positively charged residues lining the binding site homologous to the site identified for nucleotides in AAC [37]. As proposed for other MCF members, two salt bridge networks, one located on the IMS side and the other on the matrix side, serve as gates to regulate alternate access to TPP binding site [33, 36, 37].

Results

Parametrization of TPP

In order to carry out MD simulations of TPP import into the mitochondrial matrix, we have developed empirical force field parameters compatible with the all-atom CHARMM force field (version 36; [40]) for the doubly negative protonation form of TPP resulting from the negatively charged pyrophosphate moiety (charge 3-) and the positively charged thiazolium ring (charge 1 +). This protonation state was chosen on the basis of pK_a values of TPP phosphate groups predicted using the Epik software [41] (Fig. S1) calculated at the pH range value prevailing in the cytosol, IMS and mitochondrial matrix which are about 7.2, 6.8 and 7.6 respectively [42, 43].

TPP contains several unusual features that complicate parameter development. These features are located mainly on the thiazolium ring, which contains a positively charged nitrogen and a sulphur atom in a substituted five membered ring. This results in high dihedral coupling, charge complexity, uncommon atom types and thus in a high number of new parameters to be optimized. In order to reduce the number of parameters per molecule to be developed so that parameter determination would become computationally tractable, a "divide-and-conquer " strategy (M&M) was applied in which TPP was first divided into small fragments (Fig. 2A, B, C) which were successively reassembled into larger ones (Fig. 2D–E) and finally in TPP (Fig. 2F). The parameters of one of these fragments, methylpyrophosphate^{3-} (fragment C) have been previously developed and are available in the CHARMM force field [44].

The determination of the energy parameters consisted in the automatic assignment of atom types and generation of parameters by the program CGenFF followed by the optimization of those with a high penalty score by ffTK (see "Development of molecular parameters in CHARMM force field" section) [45–48].

As regards the atomic partial charges of the molecules, these were determined by the ffTK module (fragment B) with the exception of molecules resulting either from the addition of functional groups to a parent molecule (fragment A, E) or from the combination of two cyclic molecular systems (fragment D from fragment A and B) on which a previously established CGenFF protocol was applied (M&M) (Tables S1-S5 A). In particular, the atomic partial charges for 4-amino-2-methylpyrimidine (fragment A) were developed starting from the pyrimidine charges [44] and taking in account the addition of a methyl and an amino group (Table S1A). All newly emerging bonded parameters with a high penalty were optimized using ffTK (Tables S1–S4). The low penalty assigned by CGenFF to the only new improper parameter indicates that it does not require optimization (Tables S1, S3 and S5 F). No parameters required to be optimized in TPP^{2-} (Fragment F) (Table S5).

Validation of the newly developed parameters for the fragments and TPP were performed in two steps. First, a visual inspection of the 5-ns long MD trajectories of each fragment and of TPP in water did not reveal significant deviation from the planarity of both aromatic rings, bond lengths and valence angles. Second, for TPP, the accuracy of the parameters was also assessed by comparing the IR spectrum calculated from MD simulations with the experimental FTIR spectrum (M&M). The calculated and experimental spectra are in good agreement for wavenumbers lower than 2000 cm^{-1} which are attributed mainly to ring breathing, stretching modes between heavy atoms and CH_n bending modes (Fig. 3, Table S6). For wavenumbers higher than 2800 cm^{-1}; in the C–H, N–H and O–H bond stretching region, the peaks in the calculated IR spectrum present differences in wavenumbers up to 30 cm^{-1} (Table S6). This difference could be due to the harmonic potential approximation in the force field bonded term that breakdowns at higher frequencies. However, these vibrations are thought not to have a significant influence on the essential dynamics of biomolecules. For this reason, the length of hydrogen-carrying bonds is often fixed in MD simulations, as in the VDAC and TPPT simulations carried out in this study.

The calculated peak for symmetric stretching NH_2 (3096 cm^{-1}) presents a large difference with the experimental one which could be due to the high sensitivity of O–H or N–H stretching modes to solvent interactions. The broad peak located around 3300 cm^{-1} in the experimental spectrum characteristic of O–H stretching could arise from water molecules that are not accounted for in the theoretical

Journal : Large 10822 | Article No : 414 | Pages : 22 | MS Code : 414 | Dispatch : 11-8-2021

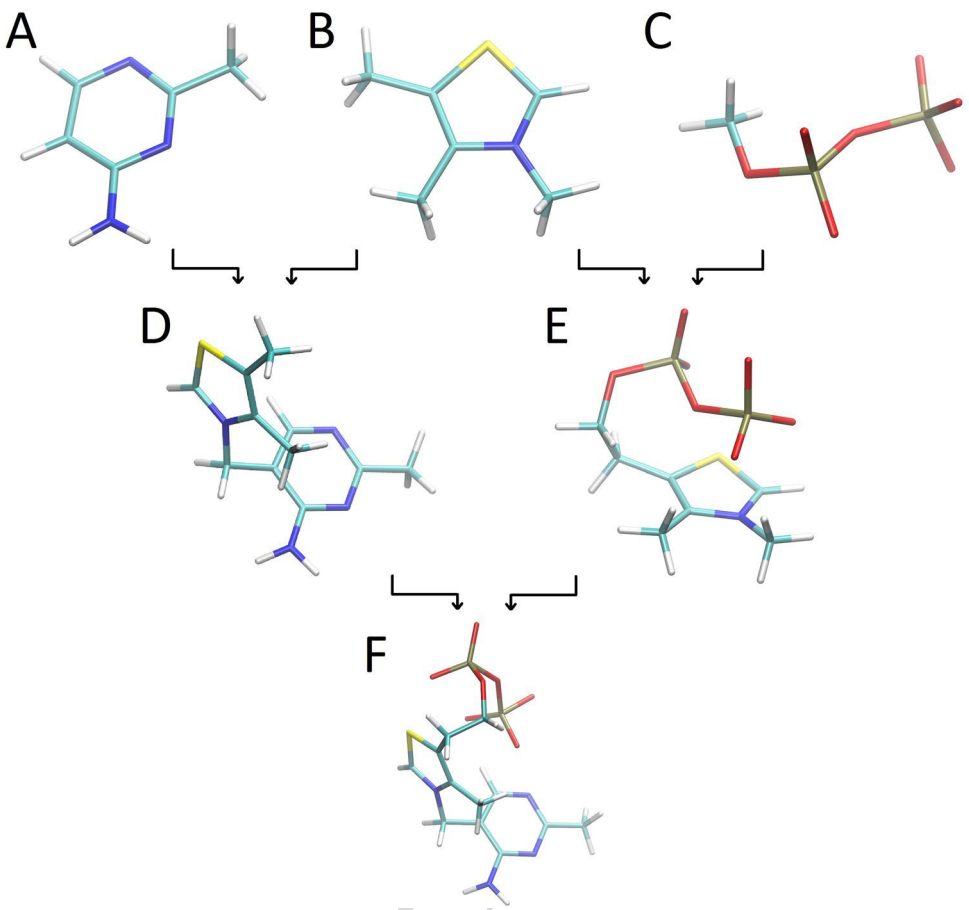

Fig. 2 "Divide-and-conquer approach" for TPP parametrization. TPP was fragmented into three model compounds (**A**–**C**). Only fragment **A** (4-amino-2-methylpyrimidine) and **B** (trimethylthiazolium^{1+}) required new bonded parameters to be determined. Fragments **A/B** and **B/C** were assembled into thiamine^{+} (fragment **D**) and dimethylthiazoliumpyrophosphate^{2-} (fragment **E**) respectively. New bonded parameters were also determined for these two fragments. Finally, fragments **D** and **E** were merged to form TPP^{2-} (fragment **F**). This step did not require any further parameter optimization. The molecular structure of the compounds is shown as sticks colored by atom type (nitrogen—blue, oxygen—red, phosphorus—gold, sulfur—yellow, carbon—cyan and hydrogen—white)

spectrum or from a small amount of protonated phosphate in TPP as the pH of the sample was 6.4. Overall, our set of optimized parameters predicts the vibrational phenomena quite well in particular in regions relevant to our MD simulations. This validates our optimized parameters for TPP^{2-} and these values were therefore used in the following simulations.

TPP import into the mitochondrion

Using the validated force field parameters of TPP^{2-}, we investigated its import into the mitochondrial matrix using MD simulations. First, we simulated the translocation of a TPP molecule through VDAC, the major pore for the permeation of metabolites through the MOM. In a second step, we simulated the transport of TPP through the MIM by its specific carrier TPPT.

Apart from the possibility that TPP may be bound to Mg^{2+} in solution [49], nothing is known about the chelation status of TPP in the different compartments of the cell or during its transport across the mitochondrial membranes. More data is available for the chelated forms of ATP, analogous to TPP. In particular, it has been shown that the permeation of ATP by VDAC through the MOM is not affected by the presence of magnesium [9] and that ATP is known to be transported through the MIM by its specific transporter, AAC, in the Mg^{2+}-free form [50, 51] although it is complexed by Mg^{2+} in the cytosol and the mitochondrial matrix [52]. Therefore, in view of the limited data available, we have simulated the transport of TPP across VDAC and TPPT both in its magnesium free (Mg^{2+}-free) and bound form (Mg^{2+}-bound).

TPP permeation through VDAC

By analogy with ATP it can be assumed that TPP flow through VDAC is rather low [53]. Therefore, to speed up

Journal : Large 10822 | Article No : 414 | Pages : 22 | MS Code : 414 | Dispatch : 11-8-2021

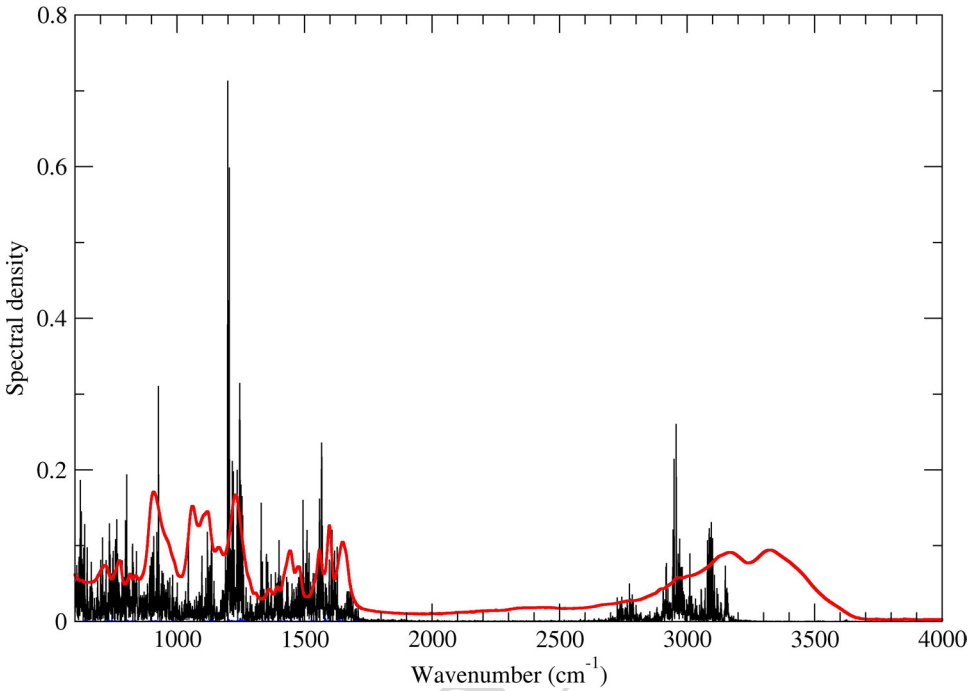

Fig. 3 Comparison of theoretical and experimental spectrum of TPP. Experimental FTIR spectra (red) and theoretical IR (black) spectral density. The ordinate axis represents the relative absorption; the magnitude of the peaks has no physical meaning. Rather, the existence of a peak at an appropriate wavenumber, representative of a vibrational phenomenon, is the main point of comparison. The spectra were obtained as described in M&M

transport, MD simulations of TPP translocation were performed with a TM voltage of 500 mV, as a previous study showed that applying such a value allowed the observation of ATP permeation through the VDAC [9]. This relatively high value of 500 mV may raise the question of maintaining the integrity of the lipid membrane. However, MD studies have reported that the electroporation process starts to occur in a POPC bilayer at values above 2 V [54, 55] and thus beyond the potential value imposed here. Furthermore, in our simulations, the transmembrane potential is applied by adding a force to all atoms carrying a charge proportional to the constant electric field perpendicular to the membrane plane. We therefore ensured that the integrity of VDAC structure is maintained throughout the simulations by calculating the root mean square deviation (RMSD), which measures the distance between conformations generated along the trajectories. The RMSD calculated along 100 ns trajectories obtained under a 500 mV potential reaches at most 2.5 Å, a value considered very close to the reference structure [56]. Of the 10 Mg^{2+}-free and 10 Mg^{2+}-bound MD simulations of TPP permeation, three and two complete permeation events were observed, respectively (Fig. 4A). All other simulations show a partial translocation of TPP. In all simulations TPP primarily visits, independently of the presence of magnesium, two regions of the pore (Fig. 4B and Fig. S2A-B), which correspond to areas above and below the N-terminal α-helix, located approximately halfway up the channel. In comparison, ATP has been shown to occupy mainly one of these two regions, the one just below the α-helix (Fig. S2C). In Mg^{2+}-bound simulations TPP appears more evenly distributed along the pore compared to the Mg^{2+}-free TPP simulations (Fig. 4B).

During its migration through the channel, TPP mainly forms ionic interactions via its phosphate group with several basic residues: K12, R15, K20, K115 and R139 (Fig. 5A–B). Three of these residues (K12, R15 and K20) located on the N-terminal α-helix were reported in previous studies as key residues for translocating metabolites through VDAC [9, 57, 58]. The other residues (K115 and R139) are approximately aligned on one side of the barrel facing the helix (Fig. 5C) accompanying TPP through its translocation. The positions of all these basic residues along the pore (Fig. 5C) as well as their flexibility given by their relatively long side chains were found to act so as to facilitate the migration of TPP across VDAC. This sweeping mechanism is illustrated, as an example, for R15, (Fig. 5D). No other types of interactions (hydrogen bonds, cation-π, π-π) formed by TPP with VDAC residues occur significantly, consistent with the previously obtained data on ATP [9]. The permeation of TPP through VDAC is thus mainly promoted by electrostatic interactions between the phosphate groups and protein basic residues. Most of these basic residues are highly conserved or only exchanged with similar amino acids (Table S7), suggesting their possible involvement in the permeation of TPP through VDAC in all kingdoms.

In the Mg^{2+}-free TPP simulations, TPP is observed to migrate through VDAC bound to one or two sodium ions except in one area just above the N-terminal helix Fig. S3A). In this region of the pore, TPP is observed to form,

Journal : Large 10822 | Article No : 414 | Pages : 22 | MS Code : 414 | Dispatch : 11-8-2021

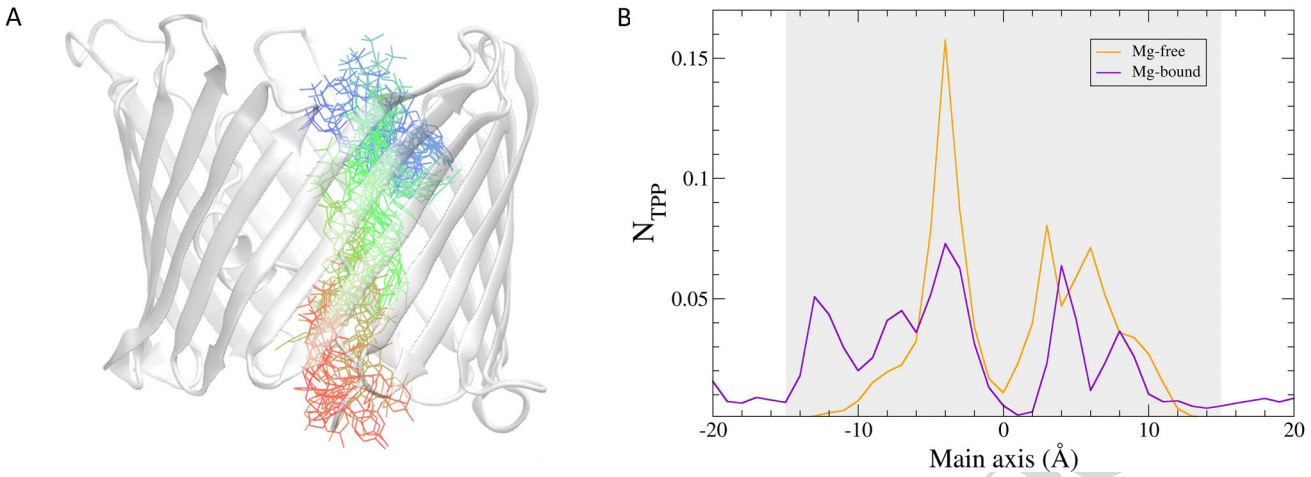

Fig. 4 Permeation of TPP through VDAC. **A** Translocation path followed by one TPP molecule during one permeation event (2.5 ns) through VDAC in a Mg^{2+}-bound MD simulation. Conformations spaced at a time interval of 0.04 ns are depicted as sticks colored from the starting position (red) to the end position (blue). The protein is shown as a transparent white cartoon. **B** Time-averaged occurrence of TPP (N_{TPP}), defined by the position of its terminal phosphorus atom, along the main axis in Mg^{2+}-free (orange) and in Mg^{2+}-bound (purple) simulations. The portion of VDAC embedded in the membrane is illustrated by a grey colored background. The cytosolic and IMS sides are at the top and bottom of VDAC respectively. The positive side of the potential is located on the opposite side of the membrane compared to the TPP starting position

in average, a high number of interactions with the basic residues (K115 and R139, Fig. 5A). In the simulations with Mg^{2+}, TPP crosses the whole barrel chelated to either Mg^{2+} or Na^{+} with a nearly constant global charge of the bound cations (Fig. S3B). Interestingly, as TPP loses its Mg^{2+} its interactions with basic residues, namely K12, R15, and K20 of the helix and sodium ions simultaneously increase (Fig. S3B and Fig. 5B). Overall, TPP is found to be almost always bound to at least one cation when it passes through the pore.

Transport of TPP by TPPT

Process of binding and of unbinding of TPP to and from the specific carrier TPPT in MIM were investigated using MD simulations. In the absence of 3D data, the TPPT structure in the c- or m-state was modelled using structures of bAAC, yAAC or mtAAC respectively [33–36] (M&M).

Modelling of the TPPT structure in the c- and m-state

The construction of reliable structural models is highly dependent on the quality of sequence alignments. Those used in this study show the conservation in TPPT of several residues involved in AAC activity [59, 60] (Fig. S4, Table S8). The sequence identity values (about 25%) are below the 30% “twilight zone” for high accuracy template-based three-dimensional modelling. Such a low level of sequence identity value is not unusual for membrane proteins, as biological membranes offer a high-contrast environment with a hydrophobic inner region and hydrophilic edges that requires only the conservation of apolar and polar segments rather than strict conservation of residues [61]. In support of this, the alignments obtained show that the positions of the predicted 6 TM regions of TPPT showed good correspondence with the helical segments identified in the bAAC, yAAC and mtAAC structures (Fig. S4). They also feature the conservation of two motifs in MCF members, the PX[DE]XX[KR] motif located in the odd-numbered TM helices on the matrix side and the [YF][DE]XX[KR] motif located in the even-numbered TM helices on the IMS side (Fig. S4) [39]. Structural data on AAC and sequence conservation analysis on MCF members have shown that each charged residue contained in each of these motifs can form up to two salt bridges between the different "repeats", thus creating a network of up to three salt bridges each between the motifs of different repeats [35, 36]. The matrix and cytosolic salt bridge networks have been proposed to play an essential role in the conformational change required for transport by being alternately formed and ruptured on the matrix and cytoplasmic side [62]. In addition, each of the matrix network salt bridges is susceptible to stabilization by braces in the form of hydrogen bonds formed by a glutamine residue located four residues away from the basic residue of the motif (PX[DE]XX[KR]XXXQ) [35]. These glutamine braces would help hold the salt bridge residues in place, to contribute to the stability of the c-state and to participate in the prevention of the c-state to m- state conversion in the absence of substrate binding [36]. Two of the three repeat motifs of TPPT contain a glutamine: Q44 (TM1) and Q245 (TM5) (Fig. S4). Our 3D modelled structures of TPPT in

Journal : Large 10822 | Article No : 414 | Pages : 22 | MS Code : 414 | Dispatch : 11-8-2021

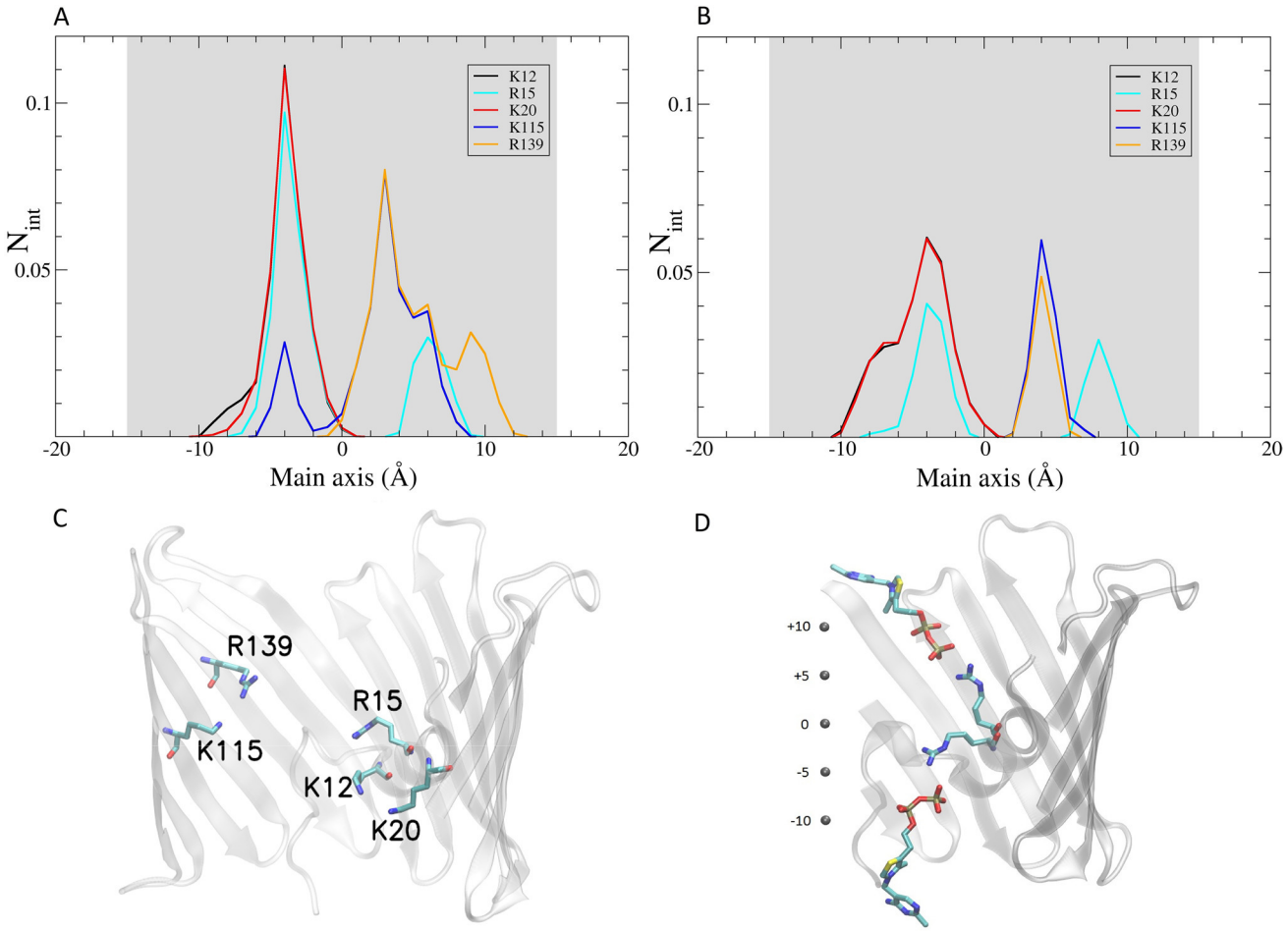

Fig. 5 Interactions of TPP with VDAC residues. Time-averaged number of interactions (N_{int}) of TPP phosphate groups with basic residues (K12-black, R15-cyan, K20-red, K115-blue and R139-orange) along VDAC main axis in (**A**) Mg^{2+}-free or in (**B**) Mg^{2+}-bound simulations. The position of TPP is defined by the position of the terminal TPP phosphorus atom. The portion of VDAC embedded in the membrane is illustrated by a grey colored background. **C** Basic residues forming interactions with TPP (as identified in **A** and **B**) are depicted as sticks and colored according to the atom-type. The protein is shown as a transparent white cartoon. **D** The sweeping mechanism of basic residue side chains by which migration of TPP through VDAC is facilitated is shown here by way of example for R15 and two of its different side chain orientations together with the corresponding positions of TPP. Residues and TPP are represented as sticks and colored according to the atom-type. Grey beads indicate the position along the main axis. The cytosolic and IMS facing sides are at the top and bottom of VDAC respectively. The positive side of the potential was located on the opposite side of the membrane compared to the TPP starting position

the c-state feature thus three salt bridges shaping the matrix network: D37-R143 (TM1-TM3), K40-D238 (TM1-TM5) and D140-K241 (TM3-TM5) (Fig. 6A, B) as well as two hydrogen bonds formed by the glutamine residues, Q44 (TM1) and Q245 (TM5) acting as braces for the residues of the matrix salt bridge network (Fig. 6A). In hTPPT the charged residues of the [YF][DE]XX[KR] motif forming the cytoplasmic network are less conserved (Fig. S4) than those of the matrix network. Only one of the two charged residues is present in two of the three repeats (K200 in TM4 and E304 in TM6) capable of forming a single salt bridge (Fig. 6C, D). The tyrosine residue contained in the [YF][DE] XX[KR] motif has also been reported to serve as props for the cytoplasmic salt bridge network [36] in the same way that the glutamines act as braces for the matrix network. In hTPPT, two of the three repeats show the conservation of the tyrosine (Y196, and Y303; Fig. S4). Consistent with the conservation of the charged residues in the [YF][DE] XX[KR] motifs, the 3D TPPT model of the m-state features a cytoplasmic network consisting of one single salt bridge formed between K200 (TM4) and E304 (TM6) (Fig. 6C, D). Y303 of the second repeat (TM6) forms a hydrogen bond with E101 (TM2) acting, in hTPPT, not as a brace but as a substitute partner for a missing salt bridge. Therefore, of the two tyrosine residues conserved in the TPPT [YF][DE] XX[KR] motif, Y196 (TM4) and Y303 (TM6), only Y196, in the m-state model, may acts as a brace for the K200-E304

Journal : Large 10822 | Article No : 414 | Pages : 22 | MS Code : 414 | Dispatch : 11-8-2021

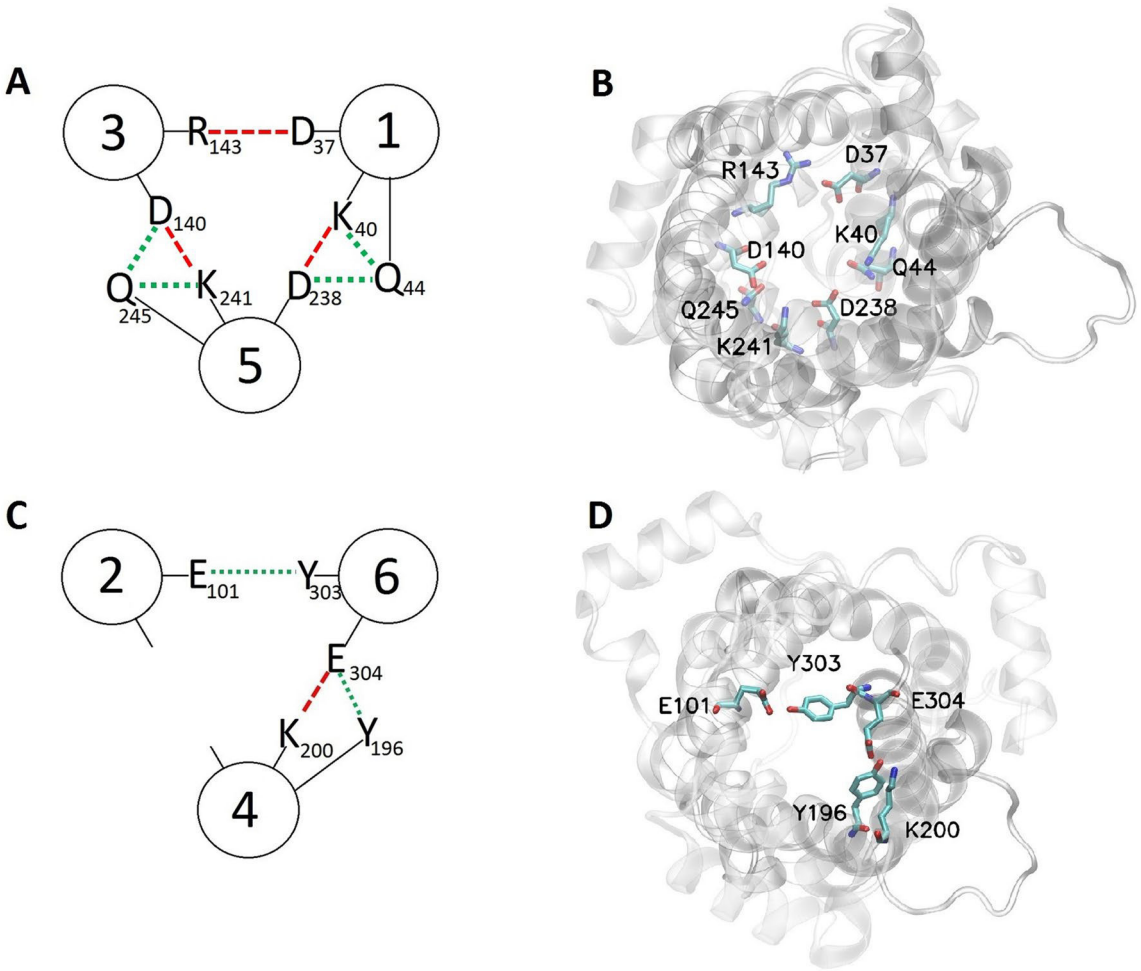

Fig. 6 Salt bridge networks and hydrogen bond braces in TPPT. The residues involved in the **A**, **B** matrix and **C**, **D** cytoplasmic salt bridge network, stabilized by their respective glutamine or tyrosine braces are shown. Salt bridges and hydrogen bonds identified in the 3D models are represented by red and green lines, respectively. The TM segments are represented as large circle and numbered. View of TPPT from the cytoplasmic side in the **B** c- and **D** m-state

salt bridge by forming a hydrogen bond with E304 and K200 (Fig. 6).

Overall, the features of our alignments as well as the formation of networks salt bridges and hydrogen bond braces contribute to the validation of our TPPT structural models.

Binding of TPP to the c-state of TPPT

Using a combination of different MD techniques, we investigated the process of binding of TPP to the c-state of TPPT. The structure of TPPT in its unbound c-state remains stable as shown by the funnel radius profile computed along MD simulations which indicates a large opening on the IMS side and an occlusion on the opposite matrix side (Fig. S5). As in the initial models (Fig. 6), the three salt bridges of the matrix network, unlike those of the cytoplasmic network, are formed, thus contributing to the stability of the c-state (Table 1A). In addition, only one of the glutamine braces (Q44) forms, in the simulations, a hydrogen bond with K40, which is intrahelical as both residues are located on the same TM, reinforcing one of the two charged residues of the salt bridge (Table 1A). As expected for the c-state, no "brace" tyrosine (for hTPPT, Y196) is observed with the exception of that formed with K200 (~40%) which has the particularity of being an intrahelical hydrogen bond (Table 1B).

TPP binding was first simulated in the absence of an external force. These simulations, performed in absence of Mg^{2+}, did not however show any entry of TPP (Table 2B). Simulations were then carried out with a TM potential difference of 500 mV as simulations with a lower potential value did not lead to binding events. Half of these simulations highlight binding of TPP which is positioned lengthwise with its phosphate group located at the bottom of the funnel and the pyrimidine and thiazolium rings oriented towards the cytoplasmic side (Fig. 7A, 8A). In the other half, TPP remains mainly hooked to an IMS loop where

Journal : Large 10822 | Article No : 414 | Pages : 22 | MS Code : 414 | Dispatch : 11-8-2021

Table 1 Formation of the matrix and cytosolic salt bridge network

A							
Observed interaction → Molecular context ↓	Matrix network			Glutamine braces			
				Q44		Q245	
	K40-D238	R143-D37	K241-D140	Q44-K40	Q44-D238	Q245-K241	Q245-D140
Unbound c-state	100	99.4	76.3	99.8	0	2.9	20.6
Bound c-state	98.4	95.3	51.8	28.8	0.03	0.2	64.2
Bound m-state	0	0	0	0	0	32.3	0
Unbound m-state	25.4	21.2	0	14.7	0	19.3	4.5

B				
Observed interaction → Molecular context ↓	Cytoplasmic network		Tyrosine braces	
			Y196	
	K200-E304	E101-Y303	Y196-K200	Y196-E304
Unbound c-state	0	0	42.4	0
Bound c-state	0	0	31.5	0
Bound m-state	30.5	55.4	26.5	7.6
Unbound m-state	58.1	78.2	54.8	42

The percentage of the different interactions (Table S11) identified for the (A) matrix and (B) cytoplasmic salt bridge networks and hydrogen bonds formed by glutamine and tyrosine braces in the c- and m-state simulations was calculated for the unbound c-state, bound c-state, bound m-state, and unbound m-state. This percentage was calculated by dividing the number of conformations featuring the type of interactions considered by the total number of conformations in the last ns of the trajectory. of the " unbound c-state of TPPT", "TPP binding to the c-state", "c-state to m-state transition", and "Release of TPP from the m-state" simulations respectively (M&M)

Table 2 Overview of the performed MD simulations

A	Simulated system → studied process ↓	VDAC (Mg^{2+} free)	VDAC (Mg^{2+}-bound)
	Total simulation time	1000-ns	1000-ns
	TPP permeation	100-ns with 500 mV (vMD: 10)	100-ns with 500 mV (vMD: 10)
B	Simulated system → studied process ↓	TPPT (Mg^{2+} free)	TPPT (Mg^{2+}-bound)
	Total simulation time	975-ns	190-ns
	unbound c-state of TPPT	20-ns (cMD: 2)	
	TPP binding to the c-state	20-ns (cMD: 4) 15-ns with 500 mV (vMD: 1) 20-ns with 500 mV (vMD: 9) 30-ns with 500 mV (vMD: 2) 50-ns with 500 mV (vMD: 2)	20-ns with 500 mV (vMD: 7) 50-ns with 500 mV (vMD: 1)
	Release of TPP from the m-state	20-ns with 500 mV (vMD: 4) 20-ns (tMD:14)	
	unbound m-state of TPPT	20-ns (cMD: 1)	

A. VDAC and B. TPPT system. The length and type (classical: c, applied transmembrane potential: v, or targeted: t, of simulation and the number of trajectories (in brackets) are given. The studied process is also indicated

it forms privileged interactions with two basic residues (R116 and K200) located at the end of two TMs (Fig. S6). One of these, K200, is a conserved residue involved in the cytoplasmic salt bridge network expected to be formed in the m-state. The same protocol (an applied TM potential of 500 mV) with Mg^{2+}-bound TPP produced no binding events, even in longer simulations (Table 2B) suggesting that only the magnesium free form of TPP is transported by TPPT in the same way as ADP/ATP is translocated by AAC [50, 63].

Along its migration process down to the binding site, the only persistent interactions formed between TPP and the

Journal : Large 10822 | Article No : 414 | Pages : 22 | MS Code : 414 | Dispatch : 11-8-2021

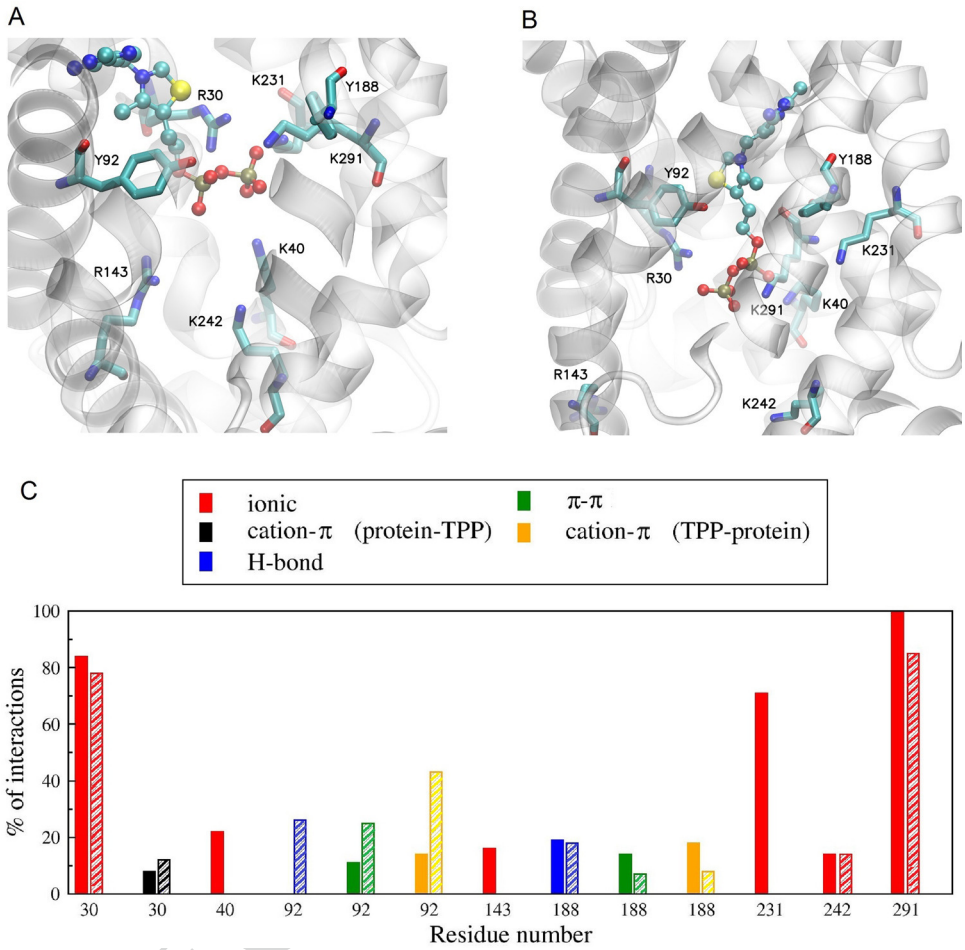

Fig. 7 Binding of TPP in the c- and m-states. View of TPP and its neighboring residues in the binding site of TPPT in the c-state (**A**) and the m-state (**B**). The protein is represented as a transparent grey cartoon and its residues represented as sticks, TPP is illustrated using the CPK representation. Both c- and m-state conformations of TPPT are oriented with the cytosolic side of the protein upwards. A histogram based on data from Table S10 represents the percentage of the different interactions formed by the residues of the binding site (**C**). Ionic, cation-π (protein-TPP), H-bond, π-π and cation-π (TPP-protein) interactions are colored in red, black, blue, green and orange respectively with those representing the m-state being hatched

carrier are mainly ionic, with the exception of a hydrogen bond, and are formed between the phosphate groups and several protein residues (R30, R143, Y188, K231, K242 and K291: Fig. 8A, C, Table S10). These residues show a high conservation across different species (Table S8). Most of their corresponding residues in homologous AAC, with the exception of K231, were found to be important for nucleotide transport (Table S9).

In the binding site TPP is mainly anchored by ionic interactions formed between its phosphate groups and basic protein residues R30, K231, K291 and to a lesser extent K40, R143 and K242 (Fig. 8A, C, Table S10), two of which (K40 and R143) are part of the matrix salt bridge network (Fig. 6A, B).

Other interactions are also formed with R30, Y92 and Y188 to varying degrees: a hydrogen bond with its phosphate group, an interaction π-π with its pyrimidine ring and a cation-π interaction with the thiazolium ring (Fig. 7A, C, Table S10). Most of the corresponding residues in homologous AAC have also been shown to be functionally important (Table S9), with the exception of Y92 and K231. These two residues are not conserved in MCF members (Table S8); on the other hand, they are strongly conserved in TPPT carriers (Fig. S7, Table S8).

Furthermore, the transition from the unbound to the bound c-state leads to a rather strong destabilization of one (K241-D140) of the three salt bridges of the matrix network and a rather weak one of the other two (K40-D238 and R143-D37). Thus, at this stage of transport, TPP fixation does not seem to lead to a clear break in the matrix network, even if it is destabilized. The observation that three residues that form a significant part of the interactions with TPP in the binding site do not belong to the salt bridge network is a possible explanation for this non-complete destabilization.

Unbinding of TPP from the TPPT m-state

Unbinding of TPP from its TPPT binding pocket was simulated in a modelled TPP-bound m-state (M&M). A first set of simulations carried out with an applied 500 mV voltage did not allow the release of TPP from the binding site to be observed (Table 2B). Therefore, tMD simulations were performed in which the bound TPP was targeted to different locations in the matrix side of the membrane (Fig. 8B).

Journal : Large 10822 | Article No : 414 | Pages : 22 | MS Code : 414 | Dispatch : 11-8-2021

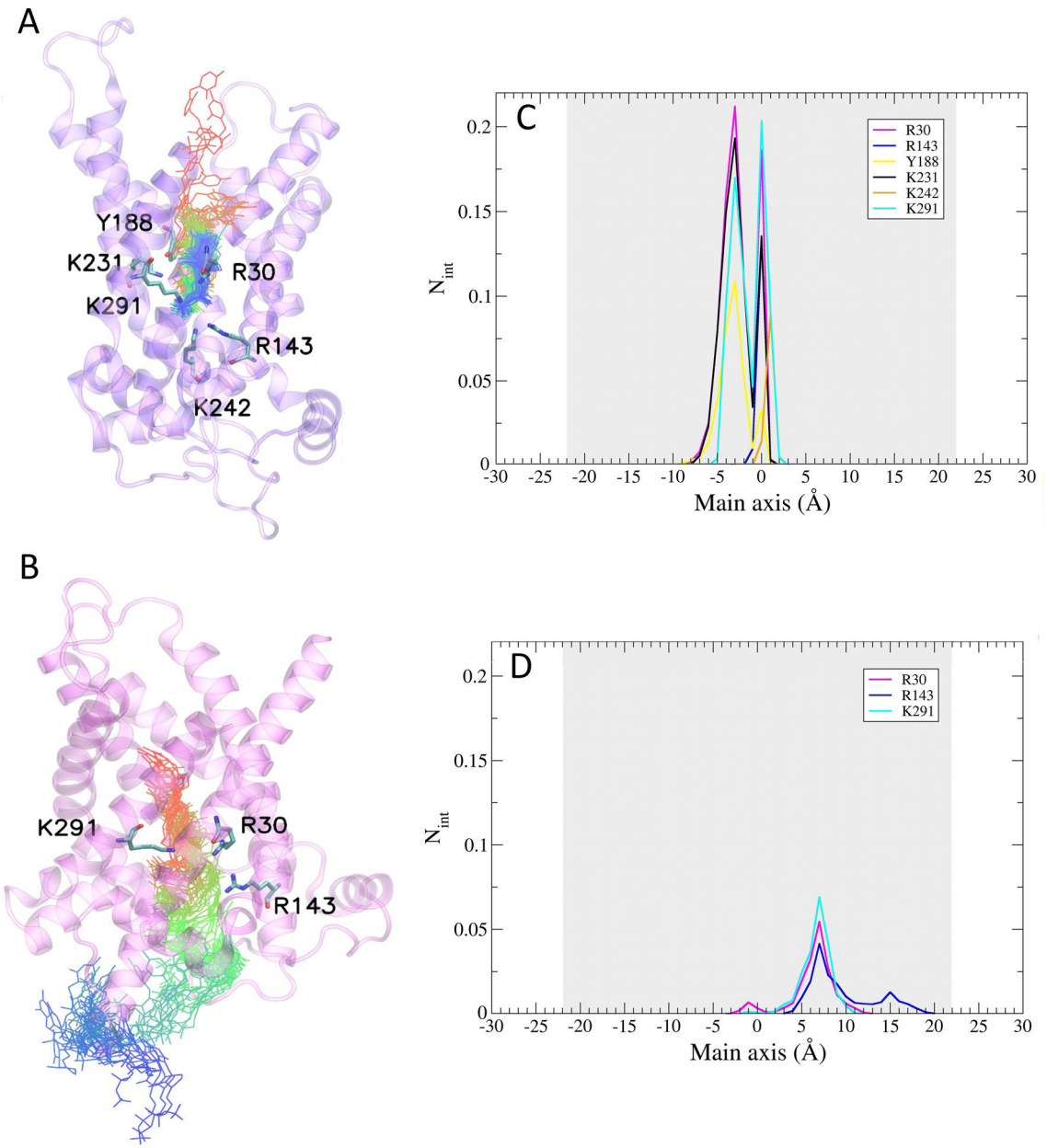

Fig. 8 Binding and release of TPP. **A**–**B** Path followed by a TPP molecule during a binding event to the c-state (**A** purple protein) and during an exit event from the m-state (**B** pink protein). TPP is depicted as sticks and colored according to a color gradient from the starting position (red) to the end position (blue) along the path in conformations spaced by 0.04-ns and important residues are shown. **C**–**D** Time-average number of interactions (N_{int}) formed between TPP phosphate groups and protein residues, ionic (R30-magenta, K40-red, R143-blue, K231-black, K242-orange and K291-cyan) and hydrogen bond (Y188-yellow) interactions, as a function of the position of the terminal phosphorus atom of TPP along the main protein axis, during simulations featuring a binding of TPP to **C** TPPT c-state and **D** during unbinding events of TPP from TPPT m-state. The portion of TPPT embedded in the membrane is illustrated by a grey colored background. The cytosolic and IMS sides are at the top and bottom of TPPT respectively. The negative side of the potential was located on IMS side of the membrane and the positive side on the matrix side of the membrane. The percentage of interaction is given by all snapshots (extracted each 2 ps) of the simulations in which the interaction is formed divided by all snapshots

Journal : Large 10822 | Article No : 414 | Pages : 22 | MS Code : 414 | Dispatch : 11-8-2021

Upon the exit of TPP, no persistent interactions formed by the transporter with TPP were found except for interactions in the binding site (R30, R143 and K291) that are lost upon disengagement of TPP (Fig. 8B, D).

After TPP is released into the matrix, a slight closure of TPPT structure is observed in some but not all simulations as shown by the calculated radius profile of the funnel (Fig. S5). This contrasts with the stability of the unbound and bound c-states as well as the bound m-state (Fig. S5). The closing of the funnel is concomitant to a partial re-formation of the matrix salt bridges as well as of the hydrogen bonds with the glutamine braces (Table 1). These observations point to a less stable unbound m-state relative to the other three states.

Discussion

In this study, the mitochondrial import of TPP through VDAC, the main channel of MOM, and TPPT, a specific transporter of the MIM, was explored using a combination of simulations at atomic level. For this purpose, CHARMM force field parameters have been developed for TPP using the CGenFF parameter database as a starting point in a "divide and conquer" strategy (Fig. 2). Comparison of the computed and experimental IR spectra as well as water phase simulations indicate that the optimized parameters are capable of reproducing the structure and dynamics of TPP (Fig. 3).

Permeation of TPP through MOM

Our simulation results support the conjecture that TPP crosses the MOM by permeating through VDAC (Fig. 1A). TPP permeation through VDAC is indeed observed in the simulations but moreover, it shows strong mechanistic analogies with that of other metabolites such as ATP [9]. Among those, permeation of TPP through VDAC is mainly promoted by several ionic interactions formed by its terminal phosphate group with basic protein residues (Fig. 5). Most of these residues are conserved in the different kingdoms (Table S7), suggesting that the transport mechanism of TPP occurs in a similar way in all VDAC species. The basic residues that form the most persistent interactions, K12, R15 and K20, are also those that have been reported in previous studies to be involved in the transport of other metabolites by VDAC [7–9]. Our simulations highlight that two other residues, K115 and R139, help the permeation of TPP from the opposite side of the pore relative to the central α-helix. In addition, the simulations show a system in which these basic amino acids, through a sweeping movement of their long flexible side chains, facilitate the permeation of TPP. Such a mechanism had already been previously demonstrated in the study of the transport of other metabolites such as ATP [9]. Based on these data, our simulations support the hypothesis that VDAC is the channel that transports TPP through the outer membrane. These results on TPP also suggest the existence of weak binding sites, reinforcing the long-standing hypothesis that VDAC may play a role in the regulation of metabolite transport into and out of mitochondria [64].

Permeation of TPP through the MIM

After TPP has passed through the MOM into the IMS, it is taken over by a specific carrier, TPPT, to cross the MIM (Fig. 1A). Our overall 2 µs long MD simulations reveal that TPPT operates by an alternating-access mechanism with a single binding site. In the c-state, the negatively charged TPP is attracted to the binding site likely to be due to the electrostatic forces resulting from the excess positive protein residues there (Fig. S8).

At the binding site, TPP non-covalently binds primarily to positively charged residues by establishing ionic interactions with its phosphate groups (Fig. 7, Table S10). In addition, two aromatic residues also play a role in the binding of TPP by interacting through either hydrogen bond, cation-π or a π-π interactions.

The interactions formed by TPP are relatively as numerous in the c-state as in the m-state although distributed differently according to the type of interactions (Table S10 and Fig. 7). In the m state, there are fewer ionic interactions and, in contrast, more H-bonds, π-π and cation-π interactions. In the c-state, the negatively charged TPP is attracted to the binding site, probably due to electrostatic forces resulting from the excess of positive residues of the protein there, as shown in the isopotential contour map (Fig. S8) which suggests that a positive electrical potential is conducive to the attraction of TPP to the binding site. In the m-state, this electrostatic potential remains but is less pronounced. The reduction in the number of ionic interactions in the m-state compared to the c-state can be explained by the fact that the TPP has to be detached from TPPT to be released into the mitochondrial matrix. These observations can also be rationalized by considering that TPPT could function as a uniporter or antiporter, f.i. with thiamine monophosphate, in that the energy input required to counterbalance that of the salt bridge matrix network should be less than that required for the cytoplasmic network.

Based on the idea that, to reflect the diversity of MCF substrates which are asymmetric, the binding site of the pseudosymmetric MCF carriers should themselves be asymmetric, binding site residues were predicted from the analysis of the three repeat sequences [65]. Although this analysis identified relatively few highly conserved asymmetric residues in the cavity of TPPT it pointed to R30 (TM1), K291 (TM6) and possibly K231 (human TPPT numbering) as likely to be involved in binding with TPP

Journal : Large 10822 | Article No : 414 | Pages : 22 | MS Code : 414 | Dispatch : 11-8-2021

[65]. I41, T44 and K242 are also cited as asymmetric residues located in the binding cavity [65, 66]. After reviewing data from [65], Y92 appears also as an asymmetric residue (triplet 83 in Fig. S4 of [65]). Of these seven residues five are identified in our simulations to be involved in the binding of TPP (Table S10, Figs. 7 and 8).

Most of the residues (R30, R143, Y188, K242 and K291) forming persistent interactions with TPP in the binding site are either strictly conserved or similar in AACs (Table S9). Experiments have indeed shown that mutation of their corresponding residues in yAAC (K38, R152, Y203, R253 and R292 respectively) led to a severe impairment of nucleotide transport across the mitochondrial membrane in AAC [60]. The close similarity between the binding site of TPPT and AAC is not surprising in that human TPPT was initially identified as a deoxynucleotide transporter [5], even though its main function was eventually shown as that of TPP transport [6]. Although all MCF members have a similar structure and transport mechanism, the recognition of their substrate is specific to each transporter. In particular, TPPT substrate specificity differs from that of the AAC, a very specific ATP/ADP carrier, in addition to transporting TPP with high efficiency [67], TPPT also transports mono-, di- and triphosphate (deoxy)nucleotides with the order of effectiveness: NMP > NDPs > NTPs with a slightly lower efficiency for the nucleobases other than adenine [39]. MD studies of the binding of ADP to bAAC revealed residues, K22, R79, R235 and R279 (bAAC numbering) as the binding partners of the phosphate moiety at the bottom of the binding cavity [67–69]. Comparison of these residues with those involved in the binding of TPP phosphates to TPPT reveals three differences. One is the leucine L88 which corresponds to R79 involved in the bAAC substrate selectivity of bAAC (Table S9). The second is Y92 which aligns with a threonine in the AACs and is engaged in numerous interactions with TPP that are related to its aromaticity. The third, K231 of TPPT, coincides with a glycine (G224) in bAAC. The substitution of glycine for lysine promotes a reduction in the size of the bottom of the binding cavity that may affect the recognition of certain nucleotides. As regards the thiamine moiety, it occupies various positions in the simulations of the c-state, all oriented towards the IMS, which differs, in this respect, from the position of the nucleoside part of the ADP observed in AAC [67, 68]. These divergent observations could be related to the difference in polarity between the adenine nucleoside and the thiamine: the former being characterized by a relatively low dipole moment in particular compared to other nucleobases [70] and the latter having a positive charge carried by the thiazolium moiety. Overall the differences observed at the level of the phosphate and of the thiamine binding could provide a rational basis for the specificity of TPPT for TPP.

Permeation of TPP through the MIM: the importance of two salt bridge networks

MCF members feature a network of matrix and cytoplasmic salt bridges located, respectively, on either side of the binding site that alternately form and break during transport to allow the conformational change to take place [65, 66, 71, 72]. The 1.1-μs long MD simulations of TPPT corroborate that the matrix and cytoplasmic network of salt bridges act as key elements in the stabilization of the c- and m-states (Table 1). The matrix network consisting of three salt bridges, each connecting a pair of odd-numbered helices, are formed persistently in our trajectories of the c-state, featuring however a slight destabilization upon binding of TPP, and breaks in the m-state. The "bracing" glutamine residues that would support this network are formed in a non-persistent manner. The only persistent hydrogen bond is formed within the same TM between $I-i+4$ residues (Table 1A). As far as the cytoplasmic network is concerned, the one of TPPT is distinctly weaker than the matrix network, on the one hand because it consists of only a single salt bridge (K200-E304) and of a hydrogen bond (E101-Y303, replaces a salt-bridge; Fig. 6C) relative to the three salt bridges of the matrix network (Fig. 6A) and on the other hand because the only cytosolic salt bridge stabilizes at most 60% of the m-state conformations (Table 1B). The tyrosine system bracing the cytoplasmic network is also more fragile because it consists of only one tyrosine brace formed by Y196 which is only supporting the K200-E304 salt bridge to at most 40% (only in the unbound m-state, Table 1B).

An energy profile of TPP transport by TPPT has been elaborated using the data from our simulations following a semi-quantitative approach [65] (Figs. 7, 9, Table S12). It relies on two contributions: one comes from the energies of the matrix and cytoplasmic salt bridge networks reinforced by hydrogen bonds formed by the glutamine or tyrosine braces, respectively, as these elements appear to be those retained among the MCF members [35, 37]. The other comes from the energy provided by the substrate binding as it should lower the activation barrier of the transition state and which should be optimal in the occluded state [73].

Regarding the salt bridge network contribution (Table S12), our data show that the matrix network is significantly stronger in the c-state simulations than the cytoplasmic salt bridge network is in the m-state simulations. In the bound states, several interactions (mainly ionic, cation-π, and π-π, and H-bonds) between TPP and protein residues (Fig. 7, Tables S10 and S12) result into an energy input that may lower the energy barrier required to facilitate the

Journal : Large 10822 | Article No : 414 | Pages : 22 | MS Code : 414 | Dispatch : 11-8-2021

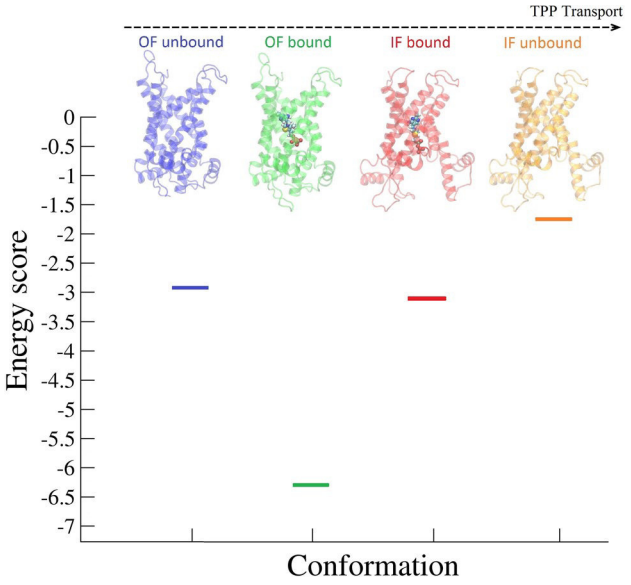

Fig. 9 Energy diagram of the different TPPT states. The semi-quantitative energetic scores, represented as straight lines, were computed for each TPPT state by assigning the value of 1 to each salt bridge and of 0.5 to each other type of interactions weighed by its occurrence (Table 1, S10) along the trajectories and summing over those formed by the ligand in the binding site (Table S10) or between the residues participating in the salt-bridge network and the corresponding braces (Table 1, Table S12). The unbound c-state, bound c-state, bound m-state and unbound m-state are shown as ribbon colored in blue, green, red and orange, respectively, above the energy diagram. The flow of the transport cycle is indicated by a dashed arrow. The cytosolic and IMS sides are at the top and bottom of TPPT respectively

transition from the c-state to the m-state and thus induce the transport of TPP into the mitochondrial matrix.

The low energy level of the cytoplasmic network could facilitate the transition from the m- state to the c-state in the absence of substrate resulting in a net import of TPP to the mitochondrial matrix as suggested elsewhere [37, 65]. Also in support of the uniporter function of TPPT is the slight closure of the TPPT structure in the m-state with a concomitant partial reformation of the matrix salt bridges as well as glutamine hydrogen bonds, which is in contrast to the stability of the c-state (Table 1).

To date, however, uniporter activity has only been clearly demonstrated for yeast TPPT [39]. Another reason for this energy weakness could have its origin in the TPP/TMP exchange activity of TPPT [6]. Although the export of TMP was not examined in this study, our simulation data shed light on the energetic mechanism of TPPT as an antiporter. Indeed, the binding of TPP in the m-state is mainly determined by the exploitation of its full negative charges. It can therefore be assumed that the energy input provided by TMP binding will be less than that provided by TPP. This input should nevertheless be sufficient for the transition from the TMP-bound m-state to the c-states in view of the lower energy required for the rupture of the cytoplasmic salt bridge network.

Mg co-transport

Although magnesium is a requirement for mitochondrial TPP utilizing enzymes, it is not known whether Mg^{2+}-TPP complexes are transported across mitochondrial membranes. Regarding the transport through VDAC, our simulation data suggest that even if TPP complexed with Mg^{2+} penetrates the channel, magnesium detaches during permeation, mainly where the channel is marked by a shrinkage due to the presence of the helix in which several basic residues are present with which TPP establishes many interactions (Fig. 4). This contrasts with our previous study on ATP permeation, where no significant difference could be found between the transport of the nucleotide complexed or not to the cation [9]. This different behavior could be due to the difference in the full charge carried by each of the translocated species.

The observations made for translocation through VDAC contrast with those of the transport of TPP by TPPT. In the latter, the complex Mg^{2+}-TPPT is not transported. The data show that the interactions of TPPT with TPP mainly take advantage of the full charges carried by TPP phosphates without the intervention of Mg^{2+}, as previously observed for ATP [50, 63]. In this, the pattern of interactions observed for TPP in TPPT binding site differs from that established by cytosolic or mitochondrial enzymes using TPP.

In summary, the import of TPP from the cytosol to the matrix is an essential event required for certain mitochondrial functions to take place that involves its transport across both mitochondrial membranes. This MD simulation study explored first the mechanism of TPP permeation by VDAC, the main conduit of the mitochondrial outer membrane, and highlighted the role of clusters of basic residues in the selectivity mechanism. A particular group of these residues located in the N-terminal helix represents a major selectivity filter for TPP. In this, similar to what has been suggested for ATP in previous studies, this group could provide a binding site and contribute to the limiting step of metabolite transport.

During the passage through the MIM stage, TPP binding at the main TPPT site is promoted by interactions formed by several basic residues that are observed to be conserved in the clade of adenine nucleotide-like transporters belonging to the MCF members. The specificity of TPPT, which differentiates it from the other transporters of this group, is ensured by two residues in particular which are conserved in the family of thiamine transporters. The opening and closing of the transporter are coupled with the alternating

Journal : Large 10822 | Article No : 414 | Pages : 22 | MS Code : 414 | Dispatch : 11-8-2021

formation and rupture of two networks of salt bridges located on the matrix and on the cytoplasmic sides. The energy of these networks combined with the binding energy input allows TPPT to be classified either as an exchanger or as a uniporter.

Material and methods

Development of molecular parameters in CHARMM force field

The parameters of TPP have been determined in the CHARMM36 force field [40]. This force field uses the following potential energy function that is a sum of bonded and nonbonded terms (Eq. 1):

$$E\left(\vec{R}\right) = \sum_{bond} K_r\left(r - r_0\right)^2 + \sum_{angle} K_\theta\left(\theta - \theta_0\right)^2 + \sum_{Urey-Bradley} K_{UB}\left(S - S_0\right)^2 + \sum_{dihedral} K_\varphi(1 + cos(n\varphi - \delta)) + \sum_{improper} K_\omega\left(\omega - \omega_0\right)^2 + \sum_{nonbonded\ pair}\left\{\varepsilon_{ij}^{min}\left[\left(\frac{r_{ij}^{min}}{r_{ij}}\right)^{12} - 2\left(\frac{Rr_{ij}^{min}}{r_{ij}}\right)^{6}\right] + \frac{q_i q_j}{4\pi\varepsilon_0\varepsilon r_{ij}}\right\} \quad (1)$$

The first five terms describe bonded energy contributions with K_r, K_θ, $K_{U\text{-}B}$, K_φ and K_ω being the force constants for bond stretching, angle bending, Urey–Bradley interactions, dihedral and improper dihedral rotation, respectively. The term r and θ represent the values of the bond length and bond angle, S, the Urey–Bradley distance, φ, the dihedral angle, n, the multiplicity, δ, the phase angle and ω, the improper dihedral angle. r_0, θ_0, S_0 and ω_0 are the equilibrium values. The last term contains two different nonbonded energy contributions in which r_{ij} represents the distance between two atoms i and j. In the Lennard–Jones energy term, ε_{ij}^{min} is the depth of the Lennard–Jones energy well and r_{ij}^{min} the distance at which the energy value reaches its minimum. In the electrostatic part of the nonbonded term, q_i and q_j represent the respective charge of the atoms i and j, ε and ε_0 correspond to the dielectric constant of the medium and to the value of the vacuum permittivity, respectively.

Calculations to derive the parameters to be optimized were performed as follows (Fig. 10). Atom types were assigned using the CGenFF program [45, 46] via the Parachem web server (https://cgenff.umaryland.edu/). Initial guesses for parameters (charges, bonds, angles, and dihedral terms parameters) were generated by analogy with the CGENFF program. An exception was made for the partial charges of molecules resulting from the addition of simple functional groups on compounds with optimized parameters as they usually require minimal or no optimization. In that case, guidelines in the CHARMM force field protocol were applied [44]. The partial charges, bond, angle, and dihedral parameter values obtained by analogy via CGENFF with a penalty score higher than 10, indicating that analogy is poor, were brought to an optimization process using the ffTK plugin of VMD [47, 48].

Lennard–Jones parameters (Eq. 1) for which direct transfer from available parameters is generally adequate, were taken directly from CGenFF for all molecules. The same procedure was followed for Urey-Bradley and improper angles parameters (Eq. 1) as ffTK does not currently provide support for their optimization.

For molecule parameters requiring optimization via ffTK (Fig. 10), the first step was to optimize the geometry of the molecule using quantum mechanics (QM) calculations at the MP2/6-31G* level. In a second step, for molecules for which no reliable parameters could be derived by analogy, the partial atomic charges were optimized by QM calculations performed at HF/6-31G* level of theory to reproduce interactions of each molecule with water molecules. In the third step, bond and angle parameters were optimized against the QM Hessian matrix of second derivatives of energy with respect to coordinates calculated at the MP2/6-31G* level of theory. From this matrix, a QM potential energy surface (PES) was determined for comparison with the molecular mechanics (MM)-derived PES. QM and MM PES were matched and upon fitting, the bond and angles parameters were determined. In the last step, parameters for dihedral angles were optimized to reproduce QM (MP2/6-31G*) PES generated by scanning different fixed values of the dihedral of interest while allowing the remainder of the molecule to relax. The Gaussian09 program was used for all QM calculations [74].

Validation of the new optimized parameters was carried out using MD simulations and infrared (IR) spectroscopy.

Journal : Large 10822 | Article No : 414 | Pages : 22 | MS Code : 414 | Dispatch : 11-8-2021

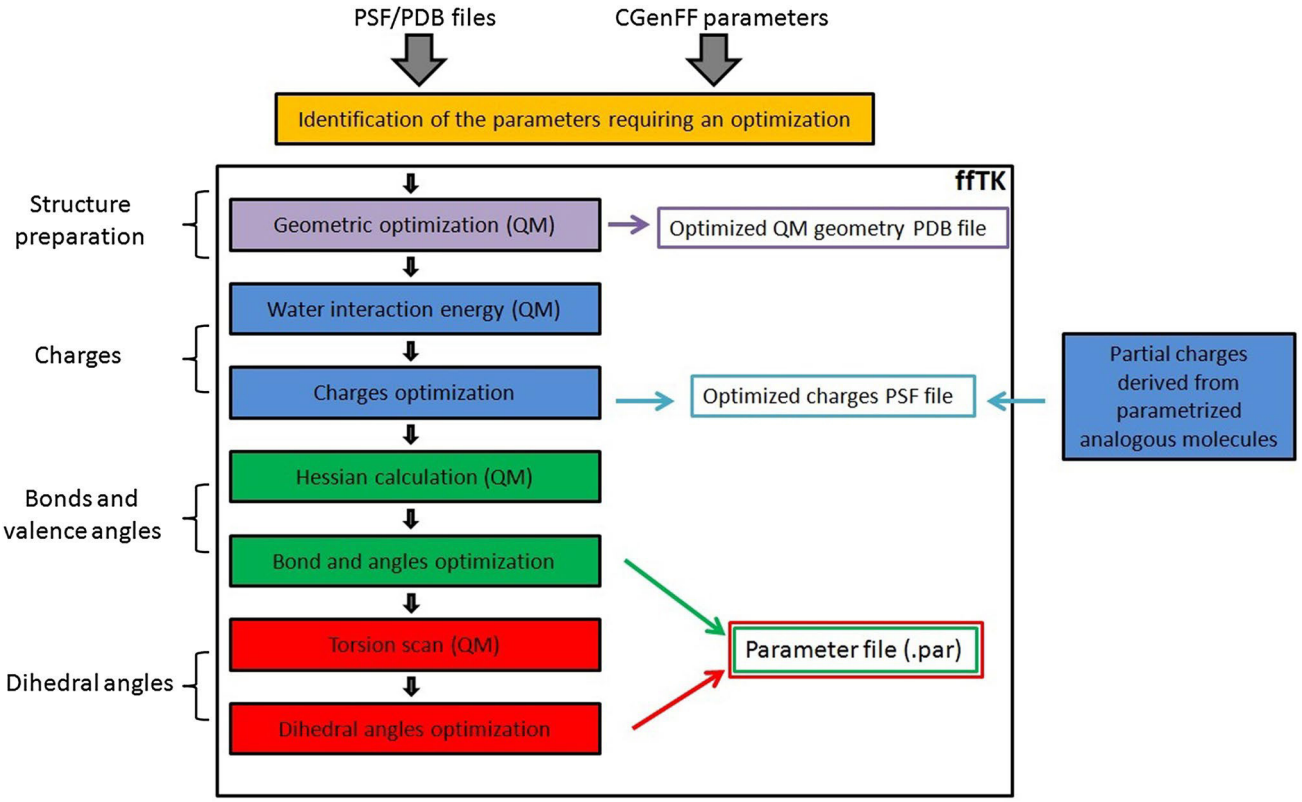

Fig. 10 Workflow illustrating the different steps followed in the parametrization of each molecule (adapted from [48]). For molecules requiring parameter optimization, the ffTK procedure was used following four steps (shown in the black frame) requiring successive calculations: geometry optimization (purple), charge optimization (blue) based on the QM calculation of the interactions of water with the molecule, optimization of bond and angle parameters (green) and dihedral angle optimization calculations (red). The output files resulting from these different steps are framed with the corresponding colors. The colored arrows indicate the origin of the optimized data. Molecules resulting from parameterized analogous molecule modifications were assigned according to a special CHARMM force field protocol (blue frame on the right)

Validation of optimized parameters

MD simulations

In order to assess the validity of the newly developed parameters we performed a visual inspection of the dynamical behavior of the solvated parametrized molecules in MD simulations. The MD trajectories were generated with the NAMD2.9 software [75] in the NPT ensemble at 300 K with a time step of 2 fs using the optimized force field. Each molecule was solvated in a cubic periodic cell (50 by 50 by 50 $Å^3$) of TIP3P water molecules using the Solvate plugin of VMD [47]. The cell contained about 3900 water molecules and was neutralized using chloride or potassium ions depending of the parametrized molecule full charge. The energy of each system with a fixed solute molecule was minimized for 1000 steps and the system equilibrated for 5 ns at 300 K. For the analysis a 5-ns long production run was then performed.

Calculated and experimental infrared spectra

The infrared (IR) spectrum was calculated using the IR spectra Density calculator in VMD from the last 100 ps of a 5-ns long MD trajectory of the doubly negative protonation form of TPP (most probable protonated form on the basis of pK_a calculations; see Results) carried out in explicit water. The MD setup parameters are identical to those of the simulations performed for the validation step (*Validation of optimized parameters; a) MD simulations*) except that the bonds involving a hydrogen were not constrained so as to observe vibrational motions related to these covalent bonds and that a time step of 1 fs was used. The default parameters of IR spectra Density calculator were used except for the time step and the maximum frequency, which were set to 1 fs and 4000 cm^{-1}, respectively.

The IR experimental spectrum of TPP was obtained using 3 mg/mL solution of resuspended TPP, with the pH adjusted to 6.4. TPP spectrum was obtained with "Attenuated Total Reflectance" (ATR) Fourier Transform IR using a Bruker

Journal : Large 10822 | Article No : 414 | Pages : 22 | MS Code : 414 | Dispatch : 11-8-2021

Equinox 55 infrared spectrophotometer equipped with a MCT Detector cooled with liquid nitrogen. 2 µL of sample was placed on the diamond ATR crystal, dried under N_2 flux and the spectrum was collected at a resolution of 2 cm^{-1} from 600 to 4000 cm^{-1} and averaged over 128 scans.

Molecular modelling of TPPT

Templates homologous to human TPPT (hTPPT) were identified by a BLASTp search [76] using the Protein Data Bank (PDB) database and the hTPPT sequence (UniProtKB accession entry: Q9HC21). The best hit structures were *Bos taurus* AAC (bAAC, [33]; PDB code: 1OKC) and *Saccharomyces cerevisiae* AAC structure (yAAC, [35]; PDB code: 4C9G), both adopting an c-state, and *Myceliophthora thermophila* AAC structure (mtAAC, [36]; PDB code: 6GCI) trapped in an m-state. Pairwise sequence alignments of each protein template with hTPPT were obtained with HHpred [77] and ClustalΩ [78]. The hTPPT transmembrane (TM) segments were predicted by HMMTOP [79] and TMPRED [80] based on the hTPPT sequence (Fig. S4).

3D models of hTPPT c-state were built by comparative modelling with the Modeller software [81] using either the bAAC or yAAC structure and the m-state was modelled using the mtAAC structure. The models were built based on the HHpred alignments because they have a higher sequence identity (21.97%, 25.74% and 24.75% for bAAC, yAAC and mtAAC respectively) and a better matching of the TM segments compared to the ClustalΩ ones. The unresolved sequence portion structures of the yAAC and mtAAC templates have been replaced by the corresponding structures in the bAAC template (Fig. S4). The structure of the sequence portions in hTPPT that do not have a match in the alignment with any of the three template structures was generated ab initio. A total of ten c-state 3D models (five with each of the two c-state template structures) and five m-state 3D models were built. Their stereochemistry was assessed with Procheck [82]. Two c-state models (one from each structure template) and one m-state model were selected as starting structure of the MD simulations based on examination of their Ramachandran plot computed with Procheck, visual inspection (elimination of structural models with knots) and the value of the objective function calculated by Modeller.

Molecular dynamics simulations

MD parameters

MD atomic trajectories were generated with the program NAMD2.9 [75] using the CHARMM36 force field [40] with CMAP [83] corrections. For TPP the parameters determined in this study were used ("Development of TPP parameters in CHARMM force field" section). All other MD parameter settings are as described elsewhere [23]. The types and length times of the MD simulations are summarized in Table 2.

System setup

The VDAC system comprises in addition to the protein about 150 POPC lipids and 9100 water molecules and contains a NaCl concentration of 0.1 M as in most experiments and theoretical studies [9, 24]. The structure of mouse VDAC (mVDAC; PDB code: 3EMN; [15]) was chosen for the simulations as it was determined at a fairly high resolution (2.3 Å). Furthermore, the sequence of mVDAC differs from the human VDAC by only four residues located in a loop of the protein. Furthermore, the mVDAC structure has been the subject of various studies that have shown agreement with numerous experimental data [9, 16, 22, 23]. The preparation of the VDAC system and the steps of equilibration preceding the production runs have been previously detailed [25].

For TPPT, three modelled structures of the human transporter, two in the c-state and one in the m-state, were prepared for MD simulations (see "Molecular modelling of TPPT" section). The three systems contained in addition to the protein each about 170 lipids and 12,000 water molecules and a NaCl concentration of 0.1 M. The protein was embedded according to its OPM orientation [84] in a lipid bilayer using the CHARMM-GUI web interface [85]. Each TPPT system was carefully equilibrated in three steps: a first 20-ns long equilibration of the fixed minimized protein was carried out to remove possible clashes between the protein and its environment without altering the protein structure. Second, a 20-ns long equilibration with the protein backbone constrained only was performed to remove possible bad contacts among the protein side chain atoms. The constrained potential was decreased from 1 to 0.5 kcal/mol/$Å^2$ after 10 ns. Third, a 20-ns long unrestrained equilibration was carried out. A 20-ns long production run followed to assess the stability of the c-state and them-state conformation(s).

Permeation of TPP through VDAC

Five different randomly chosen locations of TPP^{2-} (in its Mg^{2+} free form; hereinafter referred to as Mg^{2+}-free simulation) on the cytosolic ($z > 0$) and on the intermembrane space ($z < 0$) sides of the channel were selected as starting points to simulate TPP translocation through VDAC (Fig. S9). The cytosolic and IMS sides of the protein were defined as in [86]. The conformation of TPP was taken from the simulation of TPP alone in water (see 4.2.1). In MD simulations featuring TPP bound to Mg^{2+} (hereinafter referred to as Mg^{2+}-bound), three and two different positions of TPP^{2-} were chosen on the cytosolic or IMS side

Journal : Large 10822 | Article No : 414 | Pages : 22 | MS Code : 414 | Dispatch : 11-8-2021

respectively. Mg-TPP was considered as a non-covalent complex. The Mg^{2+} ion was initially positioned at two locations close to the β-phosphate group of TPP in analogy to its position around ATP [87] and in agreement a NMR study of TPP [49]. A 5-ns long equilibration was performed in which TPP, the ions and the protein were fixed. For each setup, a 100-ns long production run with all atoms unrestrained was generated in which a TM potential of 500 mV was imposed via an applied uniform electric field directed normally to the lipid bilayer [88] (Table 2A).

TPP binding to and unbinding from TPPT

To simulate the binding process of TPP seven different random positions of TPP^{2-} (in the absence of Mg^{2+}) were generated at the mouth of the IMS side of the two c-state hTPPT models. A 5-ns long equilibration was performed in which TPP, the ions and the protein were fixed. Binding of TPP was investigated in 14 different setups with all atoms unrestrained and an applied TM voltage of 500 mV (Table 2B). Additional 20-ns long trajectories in the absence of a TM potential were performed for two setups of each c-state TPPT structure.

The Mg^{2+}-bound MD simulation were started from 4 previous Mg^{2+}-free TPP setups generating a total of 8 Mg^{2+}-bound setups. A 5-ns long equilibration was performed in which TPP, the ions and the protein were fixed. Binding of Mg^{2+}-TPP was explored in all 8 setups (Table 2B).

To simulate the release of TPP from TPPT to the mitochondrial matrix the TPP-bound m-state was modelled. This was obtained by performing 20-ns long tMD simulations to model the transition from the substrate-bound c-state to the substrate-bound m-state for every successful TPP binding event (7 simulations; 3 for the yAAC model and 4 for the bAAC model) and using a conformation of the TPPT m-state as a target conformation. A weight of 1 kcal/mol/Å^2 was applied to the backbone heavy atoms of TM1 (residues 14 to 52), TM2 (residues 82 to 106), TM3 (residues 114 to 150), TM4 (residues 179 to 199), TM5 (217 to 243) and TM6 (286 to 305). These protein portions were selected after examining a superimposition of the c-state model and the m-state model of TPPT.

To simulate the release of TPP two types of MD simulations were performed (Table 2B) from the m-state: (i) simulations with a TM voltage of 500 mV were carried out for 20 ns for 4 out of the 7 different bound m-states produced in the c-to-m-state transition simulations. (ii) 20-ns long tMD were performed for all 8 different bound m-states in which TPP was released from the binding site to the mitochondria matrix using two different targeted random positions of TPP located in the matrix side. A weight of 1 kcal/mol/Å^2 was applied to every TPP atom.

Analysis of the trajectories

Several types of interactions were monitored in the TPPT and VDAC MD trajectories using vmd [47] or eucb [89]. These interactions and their definition criteria are listed in Table S11.

Ionic and hydrogen bond interaction occurrences between TPP and protein residues were calculated as the number of snapshots featuring a given interaction and having the phosphorus atom of the TPP β-phosphate group located in a given 1-Å-thick slice along the main axis divided by either the total number of snapshots or the number of snapshots in the same slice along the main axis. In the plots, the interactions formed with an occurrence higher or equal to 4% over all MD trajectories in at least one slice along the main axis are shown (Figs. 5 and 8).

In the TPPT simulations, a TPP binding was considered as successful when at least one phosphorus atom of the phosphate groups was within a distance smaller or equal to 4 Å of at least one of the side chain heavy nitrogen of the TPPT residues R30, K40, R143, K231, and K291. These residues were selected by analogy to the binding site defined in other MCF proteins [90–92].

To monitor the stability of the c-state and m-state as well as the c-state to m-state conformational transition of TPPT, the funnel radius of the carrier from the cytosolic to the matrix side was computed using the HOLE program [93] over the range of -20 to 20 Å along its main axis normal to the membrane (Fig. S5) and averaged over 100 configurations extracted from the last 0.1 ns of the MD trajectories.

All figures showing atomic details of proteins and molecules were generated with VMD [47].

Supplementary Information The online version contains supplementary material available at https://doi.org/10.1007/s10822-021-00414-5.

Acknowledgements M.P. is a senior research associate and E.M.K. is a postdoctoral researcher of the Fonds de la Recherche Scientifique de Belgique (F.R.S.-F.R.N.S.), Belgium. Computational resources were provided by the Consortium des Équipements de Calcul Intensif (CÉCI) and the F.R.S.-F.N.R.S. under convention 2.5020.11, together with the supercomputing facilities of the Université catholique de Louvain (CISM/UCL), the Université de Liège (ULg) and ULB.

Declarations

Conflict of interest All authors declare that they have no conflict of interest.

References

1. Bettendorff L (1994) The compartmentation of phosphorylated thiamine derivatives in cultured neuroblastoma cells. Biochim

Biophys Acta Mol Cell Res 1222:7–14. https://doi.org/10.1016/0167-4889(94)90019-1
2. Bettendorff L, Wins P (2009) Thiamin diphosphate in biological chemistry: new aspects of thiamin metabolism, especially triphosphate derivatives acting other than as cofactors. FEBS J 276:2917–2925. https://doi.org/10.1111/j.1742-4658.2009.07019.x
3. Kale S, Ulas G, Song J, Brudvig GW, Furey W, Jordan F, Kale S (2008) Efficient coupling of catalysis and dynamics in the E1 component of *Escherichia coli* pyruvate dehydrogenase multienzyme complex. Proc Natl Acad Sci USA 105:1158–1163. https://doi.org/10.1073/pnas.0709328105
4. Rosenberg MJ, Agarwala R, Bouffard G, Davis J, Fiermonte G, Hilliard MS, Koch T, Kalikin LM, Makalowska I, Morton DH, Petty EM, Weber JL, Palmieri F, Kelley RI, Schäffer AA, Biesecker LG (2002) Mutant deoxynucleotide carrier is associated with congenital microcephaly. Nat Genet 32:175–179. https://doi.org/10.1038/ng948
5. Dolce V, Fiermonte G, Runswick MJ, Palmieri F, Walker JE (2000) The human mitochondrial deoxynucleotide carrier and its role in the toxicity of nucleoside antivirals. Proc Natl Acad Sci USA 98:2284–2288. https://doi.org/10.1073/pnas.031430998
6. Lindhurst MJ, Fiermonte G, Song S, Struys E, De Leonardis F, Schwartzberg PL, Chen A, Castegna A, Verhoeven N, Mathews CK, Palmieri F, Biesecker LG (2006) Knockout of Slc25a19 causes mitochondrial thiamine pyrophosphate depletion, embryonic lethality, CNS malformations, and anemia. Proc Natl Acad Sci 103:15927–15932. https://doi.org/10.1073/pnas.0607661103
7. Rostovtseva TK, Komarov A, Bezrukov SM, Colombini M (2002) Dynamics of nucleotides in VDAC channels: structure-specific noise generation. Biophys J 82:193–205. https://doi.org/10.1016/S0006-3495(02)75386-1
8. Mannella CA, Bonner WD (1975) Biochemical characteristics of the outer membranes of plant mitochondria. BBA Biomembr 413:213–225. https://doi.org/10.1016/0005-2736(75)90105-4
9. Krammer E-M, Vu GT, Homblé F, Prévost M (2015) Dual mechanism of ion permeation through VDAC revealed with inorganic phosphate ions and phosphate metabolites. PLoS ONE 10:e0121746. https://doi.org/10.1371/journal.pone.0121746
10. Benz R (1994) Permeation of hydrophilic solutes through mitochondrial outer membranes: review on mitochondrial porins. Biochim Biophys Acta 1197:167–196
11. Homblé F, Krammer E-M, Prévost M (1818) Plant VDAC: facts and speculations. Biochim Biophys Acta 2012:1486–1501. https://doi.org/10.1016/j.bbamem.2011.11.028
12. Colombini M (1989) Voltage gating in the mitochondrial channel, VDAC. J Membr Biol 111:103–111. https://doi.org/10.1007/BF01871775
13. Bayrhuber M, Meins T, Habeck M, Becker S, Giller K, Villinger S, Vonrhein C, Griesinger C, Zweckstetter M, Zeth K (2008) Structure of the human voltage-dependent anion channel. Proc Natl Acad Sci USA 105:15370–15375
14. Hiller S, Garces RG, Malia TJ, Orekhov VY, Colombini M, Wagner G (2008) Solution structure of the integral human membrane protein VDAC-1 in detergent micelles. Science 321:1206–1210. https://doi.org/10.1126/science.1161302
15. Ujwal R, Cascio D, Colletier J-P, Faham S, Zhang J, Toro L, Ping P, Abramson J (2008) The crystal structure of mouse VDAC1 at 2.3 A resolution reveals mechanistic insights into metabolite gating. Proc Natl Acad Sci 105:17742–17747. https://doi.org/10.1073/pnas.0809634105
16. Choudhary OP, Paz A, Adelman JL, Colletier J-P, Abramson J, Grabe M (2014) Structure-guided simulations illuminate the mechanism of ATP transport through VDAC1. Nat Struct Mol Biol 21:626–632. https://doi.org/10.1038/nsmb.2841
17. Schredelseker J, Paz A, López CJ, Altenbach C, Leung CS, Drexler MK, Chen J-N, Hubbell WL, Abramson J (2014) High-resolution structure and double electron-electron resonance of the Zebrafish voltage dependent anion channel 2 reveal an oligomeric population. J Biol Chem 289:12566–12577. https://doi.org/10.1074/jbc.M113.497438
18. Hosaka T, Okazaki M, Kimura-Someya T, Ishizuka-Katsura Y, Ito K, Yokoyama S, Dodo K, Sodeoka M, Shirouzu M (2017) Crystal structural characterization reveals novel oligomeric interactions of human voltage-dependent anion channel 1. Protein Sci 26:1749–1758. https://doi.org/10.1002/pro.3211
19. Böhm R, Amodeo GF, Murlidaran S, Chavali S, Wagner G, Winterhalter M, Brannigan G, Hiller S (2020) The structural basis for low conductance in the membrane protein VDAC upon β-NADH binding and voltage gating. Structure 28:206-214.e4. https://doi.org/10.1016/j.str.2019.11.015
20. Colombini M (2009) The published 3D structure of the VDAC channel: native or not? Trends Biochem Sci 34:382–389. https://doi.org/10.1016/j.tibs.2009.05.001
21. Colombini M (1863) The VDAC channel: molecular basis for selectivity. Biochim Biophys Acta 2016:2498–2502. https://doi.org/10.1016/j.bbamcr.2016.01.019
22. Hiller S, Abramson J, Mannella C, Wagner G, Zeth K (2010) The 3D structures of VDAC represent a native conformation. Trends Biochem Sci 35:514–521. https://doi.org/10.1016/j.tibs.2010.03.005
23. Krammer E-M, Homblé F, Prévost M (2011) Concentration dependent ion selectivity in VDAC: a molecular dynamics simulation study. PLoS ONE 6:e27994. https://doi.org/10.1371/journal.pone.0027994
24. Mlayeh L, Krammer E-M, Léonetti M, Prévost M, Homblé F (1858) The mitochondrial VDAC of bean seeds recruits phosphatidylethanolamine lipids for its proper functioning. Biochim Biophys Acta Bioenerg 2017:786–794. https://doi.org/10.1016/j.bbabio.2017.06.005
25. Van Liefferinge F, Krammer EM, Sengupta D, Prévost M (2019) Lipid composition and salt concentration as regulatory factors of the anion selectivity of VDAC studied by coarse-grained molecular dynamics simulations. Chem Phys Lipids 220:66–76. https://doi.org/10.1016/j.chemphyslip.2018.11.002
26. Krammer E-M, Homblé F, Prévost M (1828) Molecular origin of VDAC selectivity towards inorganic ions: a combined molecular and Brownian dynamics study. Biochim Biophys Acta 2013:1284–1292. https://doi.org/10.1016/j.bbamem.2012.12.018
27. Krammer E-M, Saidani H, Prévost M, Homblé F (2014) Origin of ion selectivity in *Phaseolus coccineus* mitochondrial VDAC. Mitochondrion 19:206–213. https://doi.org/10.1016/j.mito.2014.04.003
28. Noskov SY, Rostovtseva TK, Bezrukov SM (2013) ATP transport through VDAC and the VDAC-tubulin complex probed by equilibrium and nonequilibrium MD simulations. Biochemistry 52:1–3. https://doi.org/10.1021/bi4011495
29. Rui H, Il Lee K, Pastor RW, Im W (2011) Molecular dynamics studies of ion permeation in VDAC. Biophys J 100:602–610. https://doi.org/10.1016/j.bpj.2010.12.3711
30. F. Palmieri, The mitochondrial transporter family (SLC25): physiological and pathological implications, (2004) 689–709. https://doi.org/10.1007/s00424-003-1099-7.
31. Drew D, Boudker O (2016) Shared molecular mechanisms of membrane transporters. Annu Rev Biochem 85:543–572. https://doi.org/10.1146/annurev-biochem-060815-014520
32. Jardetzky O (1966) Simple allosteric model for membrane pumps. Nature 211:969–970. https://doi.org/10.1038/211969a0
33. Pebay-Peyroula E, Dahout-Gonzalez C, Kahn R, Trézéguet V, Lauquin GJ-M, Brandolin G (2003) Structure of mitochondrial

ADP/ATP carrier in complex with carboxyatractyloside. Nature 426:39–44. https://doi.org/10.1038/nature02056
34. Nury H, Dahout-Gonzalez C, Trézéguet V, Lauquin G, Brandolin G, Pebay-Peyroula E (2005) Structural basis for lipid-mediated interactions between mitochondrial ADP/ATP carrier monomers. FEBS Lett 579:6031–6036. https://doi.org/10.1016/j.febslet.2005.09.061
35. Ruprecht JJ, Hellawell AM, Harding M, Crichton PG, McCoy AJ, Kunji ERSS (2014) Structures of yeast mitochondrial ADP/ATP carriers support a domain-based alternating-access transport mechanism. Proc Natl Acad Sci USA 111:E426–E434. https://doi.org/10.1073/pnas.1320692111
36. Ruprecht JJ, King MS, Zögg T, Aleksandrova AA, Pardon E, Crichton PG, Steyaert J, Kunji ERS (2019) The molecular mechanism of transport by the mitochondrial ADP/ATP carrier. Cell 176:435-447.e15. https://doi.org/10.1016/j.cell.2018.11.025
37. Ruprecht JJ, Kunji ERS (2020) The SLC25 mitochondrial carrier family: structure and mechanism. Trends Biochem Sci 45:244–258. https://doi.org/10.1016/j.tibs.2019.11.001
38. Palmieri F, Monné M (1863) Discoveries, metabolic roles and diseases of mitochondrial carriers: a review. Biochim Biophys Acta Mol Cell Res 2016:2362–2378. https://doi.org/10.1016/j.bbamcr.2016.03.007
39. Marobbio CMT, Vozza A, Harding M, Bisaccia F, Palmieri F, Walker JE (2002) Identification and reconstitution of the yeast mitochondrial transporter for thiamine pyrophosphate. EMBO J 21:5653–5661. https://doi.org/10.1093/emboj/cdf583
40. Best RB, Zhu X, Shim J, Lopes PEM, Mittal J, Feig M, MacKerell AD (2012) Optimization of the additive CHARMM all-atom protein force field targeting improved sampling of the backbone ϕ, ψ and side-chain $\chi 1$ and $\chi 2$ dihedral angles. J Chem Theory Comput 8:3257–3273. https://doi.org/10.1021/ct300400x
41. Shelley JC, Cholleti A, Frye LL, Greenwood JR, Timlin MR, Uchimaya M (2007) Epik: A software program for pKa prediction and protonation state generation for drug-like molecules. J Comput Aided Mol Des 21:681–691. https://doi.org/10.1007/s10822-007-9133-z
42. Bright GR, Fisher GW, Rogowska J, Taylor DL (1987) Fluorescence ratio imaging microscopy: temporal and spatial measurements of cytoplasmic pH. J Cell Biol 104:1019–1033. https://doi.org/10.1083/jcb.104.4.1019
43. Santo-Domingo J, Demaurex N (2012) Perspectives on: SGP symposium on mitochondrial physiology and medicine: the renaissance of mitochondrial pH. J Gen Physiol 139:415–423. https://doi.org/10.1085/jgp.201110767
44. Vanommeslaeghe K, Hatcher E, Acharya C, Kundu S, Zhong S, Shim J, Darian E, Guvench O, Lopes P, Vorobyov I, MacKerell AD (2010) CHARMM general force field: a force field for drug-like molecules compatible with the CHARMM all-atom additive biological force fields. J Comput Chem 31:671–690. https://doi.org/10.1002/jcc.21367
45. Vanommeslaeghe K, MacKerell AD (2012) Automation of the CHARMM general force field (CGenFF) I: bond perception and atom typing. J Chem Inf Model 52:3144–3154. https://doi.org/10.1021/ci300363c
46. Vanommeslaeghe K, Raman EP, MacKerell AD (2012) Automation of the CHARMM general force field (CGenFF) II: assignment of bonded parameters and partial atomic charges. J Chem Inf Model 52:3155–3168. https://doi.org/10.1021/ci3003649
47. Humphrey W, Dalke A, Schulten K (1996) VMD: visual molecular dynamics. J Mol Graph 14:33–38. https://doi.org/10.1016/0263-7855(96)00018-5
48. Mayne CG, Saam J, Schulten K, Tajkhorshid E, Gumbart JC (2013) Rapid parameterization of small molecules using the force field toolkit. J Comput Chem 34:2757–2770. https://doi.org/10.1002/jcc.23422
49. Chauvet-Monges AM, Monti JP, Crevat A, Vincent EJ (1980) Étude de l'interaction de la thiamine diphosphate avec l'ion magnésium. Biochimie 61:1301–1308. https://doi.org/10.1016/S0300-9084(80)80289-6
50. Krämer R (1980) Influence of divalent cations on the reconstituted ADP, ATP exchange. Biochim Biophys Acta Bioenerg 592:615–620. https://doi.org/10.1016/0005-2728(80)90104-8
51. Gropp T, Brustovetsky N, Klingenberg M, Müller V, Fendler K, Bamberg E (1999) Kinetics of electrogenic transport by the ADP/ATP carrier. Biophys J 77:714–726. https://doi.org/10.1016/S0006-3495(99)76926-2
52. Gout E, Rébeillé F, Douce R, Bligny R (2014) Interplay of Mg2+, ADP, and ATP in the cytosol and mitochondria: unravelling the role of Mg2+ in cell respiration. Proc Natl Acad Sci USA 111:E4560–E4567. https://doi.org/10.1073/pnas.1406251111
53. Rostovtseva T, Colombini M (1997) VDAC channels mediate and gate the flow of ATP: implications for the regulation of mitochondrial function. Biophys J 72:1954–1962. https://doi.org/10.1016/S0006-3495(97)78841-6
54. Böckmann RA, De Groot BL, Kakorin S, Neumann E, Grubmüller H (2008) Kinetics, statistics, and energetics of lipid membrane electroporation studied by molecular dynamics simulations. Biophys J 95:1837–1850. https://doi.org/10.1529/BIOPHYSJ.108.129437
55. Vernier TP, Ziegler MJ (2007) Nanosecond field alignment of head group and water dipoles in electroporating phospholipid bilayers. J Phys Chem B 111:12993–12996. https://doi.org/10.1021/JP077148Q
56. Bolhuis PG (2006) Sampling kinetic protein folding pathways using all-atom models. Lect Notes Phys 703:393–433. https://doi.org/10.1007/3-540-35273-2_11
57. Villinger S, Giller K, Bayrhuber M, Lange A, Griesinger C, Becker S, Zweckstetter M (2014) Nucleotide interactions of the human voltage-dependent anion channel. J Biol Chem 289:13397–13406. https://doi.org/10.1074/jbc.M113.524173
58. Yehezkel G, Hadad N, Zaid H, Sivan S, Shoshan-Barmatz V (2006) Nucleotide-binding sites in the voltage-dependent anion channel: characterization and localization. J Biol Chem 281:5938–5946. https://doi.org/10.1074/jbc.M510104200
59. Nury H, Dahout-Gonzalez C, Trézéguet V, Lauquin GJM, Brandolin G, Pebay-Peyroula E (2006) Relations between structure and function of the mitochondrial ADP/ATP carrier. Annu Rev Biochem 75:713–741. https://doi.org/10.1146/annurev.biochem.75.103004.142747
60. Heimpel S, Basset G, Odoy S, Klingenberg M (2001) Expression of the mitochondrial ADP/ATP carrier in *Escherichia coli*. Renaturation, reconstitution, and the effect of mutations on 10 positive residues. J Biol Chem 276:11499–11506. https://doi.org/10.1074/jbc.M010586200
61. Liang J, Naveed H, Jimenez-Morales D, Adamian L, Lin M (1818) Computational studies of membrane proteins: models and predictions for biological understanding. Biochim Biophys Acta Biomembr 2012:927–941. https://doi.org/10.1016/j.bbamem.2011.09.026
62. Kunji ERS, Aleksandrova A, King MS, Majd H, Ashton VL, Cerson E, Springett R, Kibalchenko M, Tavoulari S, Crichton PG, Ruprecht JJ (1863) The transport mechanism of the mitochondrial ADP/ATP carrier. Biochim Biophys Acta Mol Cell Res 2016:2379–2393. https://doi.org/10.1016/j.bbamcr.2016.03.015
63. Brandolin G, Doussiere J, Gulik A, Gulik-Krzywicki T, Lauquin GJM, Vignais PV (1980) Kinetic, binding and ultrastructural properties of the beef heart adenine nucleotide carrier protein after incorporation into phospholipid vesicles. Biochim Biophys Acta

| Journal : Large 10822 | Article No : 414 | Pages : 22 | MS Code : 414 | Dispatch : 11-8-2021 |

Bioenerg 592:592–614. https://doi.org/10.1016/0005-2728(80)90103-6
64. Noskov SY, Rostovtseva TK, Chamberlin AC, Teijido O, Jiang W, Bezrukov SM (1858) Current state of theoretical and experimental studies of the voltage-dependent anion channel (VDAC). Biochim Biophys Acta Biomembr 2016:1778–1790. https://doi.org/10.1016/j.bbamem.2016.02.026
65. Robinson AJ, Overy C, Kunji ERS (2008) The mechanism of transport by mitochondrial carriers based on analysis of symmetry. Proc Natl Acad Sci 105:17766–17771. https://doi.org/10.1073/pnas.0809580105
66. Robinson AJ, Kunji ERS (2006) Mitochondrial carriers in the cytoplasmic state have a common substrate binding site. Proc Natl Acad Sci USA 103:2617–2622. https://doi.org/10.1073/pnas.0509994103
67. Mifsud J, Ravaud S, Krammer E-M, Chipot C, Kunji ERS, Pebay-Peyroula E, Dehez F (2013) The substrate specificity of the human ADP/ATP carrier AAC1. Mol Membr Biol 30:160–168. https://doi.org/10.3109/09687688.2012.745175
68. Wang Y, Tajkhorshid E (2008) Electrostatic funneling of substrate in mitochondrial inner membrane carriers. Proc Natl Acad Sci USA 105:9598–9603. https://doi.org/10.1073/pnas.0801786105
69. Bidon-Chanal A, Krammer E-M, Blot D, Pebay-Peyroula E, Chipot C, Ravaud S, Dehez F (2013) How do membrane transporters sense pH? The case of the mitochondrial ADP–ATP carrier. J Phys Chem Lett 4:3787–3791. https://doi.org/10.1021/jz401847d
70. Šponer J, Leszczynski J, Hobza P (2001) Electronic properties, hydrogen bonding, stacking, and cation binding of DNA and RNA bases. Biopolymers 61:3–31
71. Miniero DV, Cappello AR, Curcio R, Ludovico A, Daddabbo L, Stipani I, Robinson AJ, Kunji ERS, Palmieri F (1807) Functional and structural role of amino acid residues in the matrix α-helices, termini and cytosolic loops of the bovine mitochondrial oxoglutarate carrier. Biochim Biophys Acta Bioenerg 2011:302–310. https://doi.org/10.1016/j.bbabio.2010.12.005
72. Cappello AR, Miniero DV, Curcio R, Ludovico A, Daddabbo L, Stipani I, Robinson AJ, Kunji ERS, Palmieri F (2007) Functional and structural role of amino acid residues in the odd-numbered transmembrane α-helices of the bovine mitochondrial oxoglutarate carrier. J Mol Biol 369:400–412. https://doi.org/10.1016/j.jmb.2007.03.048
73. Klingenberg M (2005) Ligand-protein interaction in biomembrane carriers. The induced transition fit of transport catalysis, Biochemistry 44:8563–8570. https://doi.org/10.1021/bi050543r
74. Frisch GWTMJ, Schlegel HB, Scuseria GE, Robb MA, Cheeseman JRJ, Scalmani G, Barone V, Mennucci B, Petersson GA, Nakatsuji H, Caricato M, Li X, Hratchian HP, Izmaylov AF, Bloino J, Zheng G, Sonnenberg JL, Hada M, Ehara M, Toyota K, Fukuda R, Hasegawa J, Ishida M, Nakajima T, Honda Y, Kitao O, Nakai H, Vreven T, Montgomery JJA, Peralta JE, Ogliaro F, Bearpark M, Heyd JJ, Brothers E, Kudin KN, Staroverov VN, Kobayashi R, Normand J, Raghavachari K, Rendell A, Burant JC, Iyengar SS, Tomasi J, Cossi M, Rega N, Millam JM, Klene M, Knox JE, Cross JB, Bakken V, Adamo C, Jaramillo J, Gomperts R, Stratmann RE, Yazyev O, Austin VJ, AJ, Cioslowski DJ, Gaussian 09, Revision A.1, Vol. Gaussian, Inc., Wallingford CT (2009)
75. Phillips JC, Braun R, Wang W, Gumbart J, Tajkhorshid E, Villa E, Chipot C, Skeel RD, Kalé L, Schulten K (2005) Scalable molecular dynamics with NAMD. J Comput Chem 26:1781–1802. https://doi.org/10.1002/jcc.20289
76. Altschul SF, Gish W, Miller W, Myers EW, Lipman DJ (1990) Basic local alignment search tool. J Mol Biol 215:403–410. https://doi.org/10.1016/S0022-2836(05)80360-2
77. Söding J, Biegert A, Lupas AN (2005) The HHpred interactive server for protein homology detection and structure prediction. Nucleic Acids Res. https://doi.org/10.1093/nar/gki408
78. Sievers F, Wilm A, Dineen D, Gibson TJ, Karplus K, Li W, Lopez R, McWilliam H, Remmert M, Söding J, Thompson JD, Higgins DG (2011) Fast, scalable generation of high-quality protein multiple sequence alignments using Clustal Omega. Mol Syst Biol. https://doi.org/10.1038/msb.2011.75
79. Tusnady GE, Simon I (2001) The HMMTOP transmembrane topology prediction server. Bioinformatics 17:849–850. https://doi.org/10.1093/bioinformatics/17.9.849
80. Hofmann K, Stoffel W (1993) TMbase-A database of membrane spanning proteins segments. Biol Chem 374:166
81. Šali A, Blundell TL (1993) Comparative protein modelling by satisfaction of spatial restraints. J Mol Biol 234:779–815
82. Laskowski RA, MacArthur MW, Moss DS, Thornton JM (1993) PROCHECK: a program to check the stereochemical quality of protein structures. J Appl Crystallogr 26:283–291. https://doi.org/10.1107/S0021889892009944
83. MacKerell AD, Bashford D, Bellott M, Dunbrack RL, Evanseck JD, Field MJ, Fischer S, Gao J, Guo H, Ha S, Joseph-McCarthy D, Kuchnir L, Kuczera K, Lau FT, Mattos C, Michnick S, Ngo T, Nguyen DT, Prodhom B, Reiher WE, Roux B, Schlenkrich M, Smith JC, Stote R, Straub J, Watanabe M, Wiórkiewicz-Kuczera J, Yin D, Karplus M (1998) All-atom empirical potential for molecular modeling and dynamics studies of proteins. J Phys Chem B 102:3586–3616. https://doi.org/10.1021/jp973084f
84. Lomize MA, Lomize AL, Pogozheva ID, Mosberg HI (2006) OPM: Orientations of proteins in membranes database. Bioinformatics 22:623–625. https://doi.org/10.1093/bioinformatics/btk023
85. Lee J, Cheng X, Swails JM, Yeom MS, Eastman PK, Lemkul JA, Wei S, Buckner J, Jeong JC, Qi Y, Jo S, Pande VS, Case DA, Brooks CL, MacKerell AD, Klauda JB, Im W (2015) CHARMM-GUI input generator for NAMD, GROMACS, AMBER, OpenMM, and CHARMM/OpenMM simulations using the CHARMM36 additive force field. J Chem Theory Comput. https://doi.org/10.1021/acs.jctc.5b00935
86. Tomasello MF, Guarino F, Reina S, Messina A, De Pinto V (2013) The voltage-dependent anion selective channel 1 (VDAC1) topography in the mitochondrial outer membrane as detected in intact cell. PLoS ONE 8:e81522. https://doi.org/10.1371/journal.pone.0081522
87. Watson HC, Walker NP, Shaw PJ, Bryant TN, Wendell PL, Fothergill LA, Perkins RE, Conroy SC, Dobson MJ, Tuite MF (1982) Sequence and structure of yeast phosphoglycerate kinase. EMBO J 1:1635–1640. https://doi.org/10.1002/j.1460-2075.1982.tb01366.x
88. Aksimentiev A, Schulten K (2005) Imaging alpha-hemolysin with molecular dynamics: ionic conductance, osmotic permeability, and the electrostatic potential map. Biophys J 88:3745–3761. https://doi.org/10.1529/biophysj.104.058727
89. Tsoulos IG, Stavrakoudis A (2011) Eucb: A C++ program for molecular dynamics trajectory analysis. Comput Phys Commun 182:834–841. https://doi.org/10.1016/j.cpc.2010.11.032
90. Dehez F, Pebay-Peyroula E, Chipot C (2008) Binding of ADP in the mitochondrial ADP/ATP carrier is driven by an electrostatic funnel. J Am Chem Soc 130:12725–12733. https://doi.org/10.1021/ja8033087
91. Krammer E-M, Ravaud S, Dehez F, Frelet-Barrand A, Pebay-Peyroula E, Chipot C (2009) High-chloride concentrations abolish the binding of adenine nucleotides in the mitochondrial ADP/ATP carrier family. Biophys J 97:L25–L27. https://doi.org/10.1016/j.bpj.2009.08.047
92. Kang J, Samuels DC (2008) The evidence that the DNC (SLC25A19) is not the mitochondrial deoxyribonucleotide carrier. 8:103–108. https://doi.org/10.1016/j.mito.2008.01.001
93. Smart OS, Neduvelil JG, Wang X, Wallace BA, Sansom MSP (1996) HOLE: a program for the analysis of the pore dimensions

of ion channel structural models. J Mol Gr 14:354–360. https://doi.org/10.1016/S0263-7855(97)00009-X

Journal : **Large 10822**	Article No : **414**	Pages : **22**	MS Code : **414**	Dispatch : **11-8-2021**